2023

Rotorcraft Lander Fixed to a Descending Capsule Backshell

Corey Zucker
University of Central Florida

ROTORCRAFT LANDER FIXED TO A DESCENDING CAPSULE BACKSHELL

by

COREY A. ZUCKER
B.S. University of Florida, 2019

A thesis submitted on partial fulfillment of the requirements
for the degree of Master of Science
in the Department of Mechanical and Aerospace Engineering
in the College of Engineering and Computer Science
at the University of Central Florida
Orlando, Florida

Spring Term
2023

Major Professor Michael P. Kinzel

ABSTRACT

NASA is financing a mission to study the surface of Titan, Saturn's largest moon, to investigate the terrain, chemical compositions, and potential for existent life. This mission is an exciting advancement from Mars Ingenuity, because the quadrotor lander, Dragonfly, will be the first of its kind with four coaxial rotors. Upon entry into Titan, and at near surface atmospheric conditions, Dragonfly will exit a parachute supported backshell that has shed its protective heatshield. The aerodynamics of this state are significant in comprehending the dynamics of the overall system for successful deployment into powered flight. The studies presented here examine the aerodynamic trends of the Dragonfly lander-backshell combination during Entry, Descent, and Landing (EDL), using computational fluid dynamics (CFD). More specifically, these investigations will focus on the Preparation for Powered Flight (PPF) sub-phase within EDL. The PPF mission phase begins immediately following heatshield separation, where the jettisoning of the heatshield generates an induced rotation on the lander-backshell system. This demands a "despin" capability to regain control authority prior to release of Dragonfly directly into powered flight. Preliminary evaluations of descent on Titan uncovered a suction force interaction between the rotor and lander body which opposed the current method of rotor control used for despin. The research proposes design modifications to regain control authority such as reassigning rotor control designations and altering the rotor cant. The computational model was benchmarked by comparing CFD results to experimental aerodynamic load measurements for similar backshells, bluff bodies, and rotor-body interactions. The model was adapted for Dragonfly to evaluate different descent configurations to gain a comprehensive understanding of the complex flow dynamics which is crucial in formulating strategies aimed at ensuring positive control authority of the system.

ACKNOWLEDGMENTS

I would like to thank NASA and Johns Hopkin's Applied Physics Laboratory (APL) for the opportunity to help progress Dragonfly EDL and the overall Dragonfly mission. I would also like to extend my gratitude to Dr. Michael Wright at NASA Ames Research Center and Brett Shapiro at Johns Hopkin's APL for their continued support and guidance throughout this research. Additionally, I would like to thank my graduate advisor Dr. Michael P. Kinzel and my colleagues Luis Amaya, Wayne Farrell, and Jackson Asiatico at the University of Central Florida for their supporting efforts on Dragonfly. Finally, I would like to acknowledge AIAA, more specifically the SciTech 2023 national conference in National Harbor, where I had the opportunity to publish the research contained herein.

TABLE OF CONTENTS

LIST OF FIGURES

LIST OF TABLES

CHAPTER 1: INTRODUCTION

NASA's expedition to explore Saturn's moon Titan aims to investigate the terrain, chemical compositions, and potential for life in extra-terrestrial environments. The Dragonfly mission will be the first of its kind aerial rover to explore vast distances in search of resources, such as Titan's subsurface ocean and liquid reservoirs. This constitutes significant progress from the Mars Exploration Rover (MER) missions, as Dragonfly is a unique rotorcraft lander with four coaxial rotor pairs that will release directly into powered flight. In 1944, the existence of an atmosphere on Titan was established through spectrometric analysis of reflected sunlight, in which methane was detected [1]. This discovery fueled an ongoing interest in further understanding the potential for life on Titan. Over a 13-year time period, the Cassini spacecraft gathered critical surface and atmospheric data, which has since been employed in the design and testing phases of future missions. On entry into Titan's atmosphere, Dragonfly will descend encased within an aeroshell comprised of a protective heatshield and backshell with several mechanisms to facilitate a successful landing. As depicted in the Entry, Descent, and Landing (EDL) sequence illustrated in Figure 1, the aeroshell's velocity will be reduced by main parachute deployment, which will allow for heatshield release at low speeds. This enables Dragonfly to exit its backshell directly into powered flight. NASA has previously implemented similar delivery methods for the Sojourner, Spirit, Opportunity, Curiosity, and Perseverance rovers on Mars, differing only in their final landing stages. The MER missions implemented a similar backshell-parachute design; however, the lack of flight capability of the Mars rovers required the deployment of airbags and backshell thrusters for ground impact. In comparison, the landing phase of Dragonfly is made simpler through separation of the rotorcraft from the backshell by slightly extending out the lander to obtain enough clearance to power on the rotors. The rotorcraft lander then slides off its guiderails

directly into powered flight. Understanding the complex aerodynamic interactions between backshell, lander, and rotors during descent is paramount for successful delivery of Dragonfly onto Titan.

Dragonfly will follow in the footsteps of Ingenuity as the second vertical take-off and landing (VTOL) vehicle to be deployed in an extra-terrestrial environment. Unlike its predecessor, Dragonfly will have the capability to undertake an extended relocation mission spanning hundreds of kilometers [2], [3]. This mission will also have a unique landing sequence, consisting of a Preparation to Powered Flight (PPF) and Transition to Powered Flight (TPF) phase with mid-air deployment and release of the rotorcraft. These initial phases are mission critical events within EDL and are crucial to the overall success of the mission. Following the main parachute deployment, PPF will commence with the detachment of the heatshield from the backshell which will induce an undesired rotation on the system. The lander will extend away from the backshell to carry out a "despin" maneuver, using the rotors to eliminate the induced rotation caused by heatshield release. Control authority is established once the rotors slow the system's rotational velocity to reach net-zero spin, making the despin maneuver essential for stabilizing the system before release to powered flight. Once stabilized, the lander will immediately enter a free-fall stage to distance itself from the aeroshell and pitch forward to adjust its trajectory [4]. The current studies expand on previous work and maintain focus on the events of PPF between the separation and free-fall stages [5].

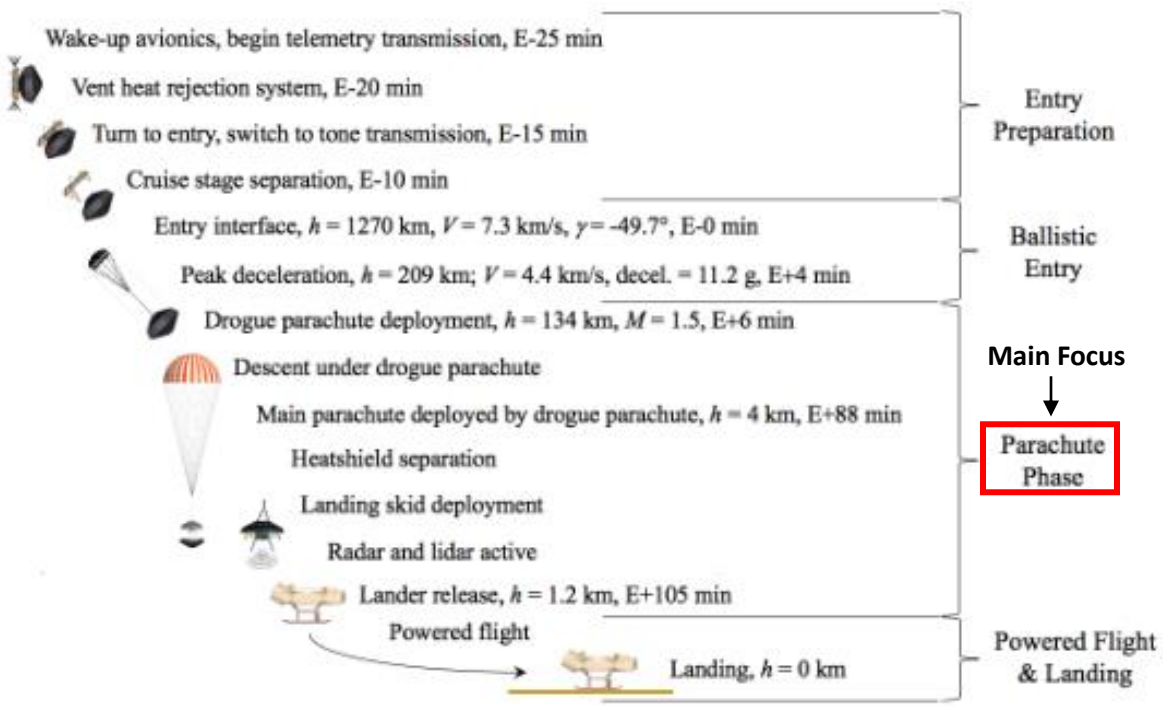

Figure 1: Mission critical EDL sequence (PPF Phase)
Picture courtesy of Dragonfly/NASA [4]

Evaluation of the rotorcraft lander will be conducted in two fixed configurations following the detachment of the heatshield. The first configuration, post-heatshield separation, is referred to as the "stowed" position in which the Dragonfly lander is stationed tightly in the backshell where the rotors are incapable of rotation as indicated in Figure 2(a). The second configuration involves extending the lander out of the backshell for rotor clearance and is referred to as the "posed" position as shown in Figure 2(b). This effort will explore the aerodynamic characteristics encountered in the posed configuration during descent conditions and provide a detailed analysis of trends in loading experienced by the Dragonfly lander-backshell system in the wind-fixed and body-fixed reference frames shown in Figure 3(a) and Figure 3(b), respectively. In preliminary efforts of the EDL mission phase, an extended aero-database was developed for descent, which found the posed configuration in certain conditions had unsuccessful despin prior to TPF. The lack

of despin control is attributed to a suction torque phenomenon between the coaxial rotors and lander body, which will be discussed in detail in Chapter 3. Extensive research currently exists on rotor-body and wake interaction for single rotor aircraft where the rotor is located directly above the lander body, similar to a helicopter configuration; however, there has been little research on quadrotor-lander interactions, especially since most quadrotors have a slim body where the effects of these interactions would be negligible. The growing interest in UAVs and rotorcraft in recent years has necessitated a rapid development of technology and research in this field. In an assessment of a quadrotor near-wall behavior by Carreño Ruiz et al. (2023), a slim-body quadrotor drone showed similar suction force behavior when placed near a solid wall [6]. This phenomenon is relatively new in quadrotor research; however, both studies show a suction force will exist between a solid vertical interface and a rotor. In the case of Dragonfly, the large bluff body of the lander acts as a vertical wall which results in a suction force on the lander body itself. This force plays a significant role in the quadrotor dynamics because the suction force coupled with the position of Dragonfly's controlling rotors results in a suction torque which opposes the desired control authority of the system for certain rotor configurations. The major objectives of these studies are to analyze the complex interactions between the coaxial rotors, lander body, and backshell at differing rotor speed settings (RPMs) and develop solutions that achieve greater despin control authority. The outcomes of this study will provide insight on EDL and atmospheric entry on other planets for future rover and exploratory missions.

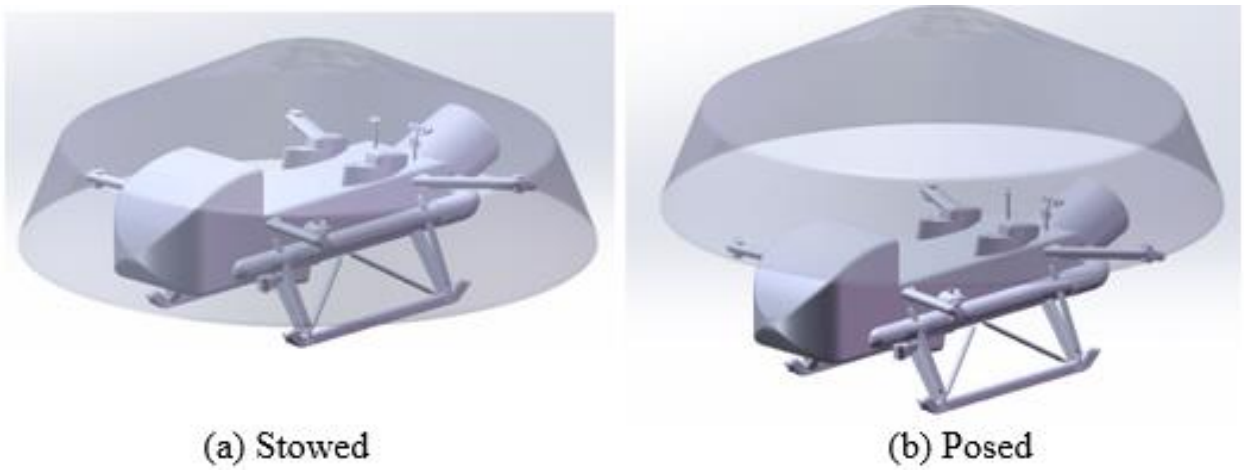

Figure 2: Dragonfly configurations in the stowed and posed configurations of PPF

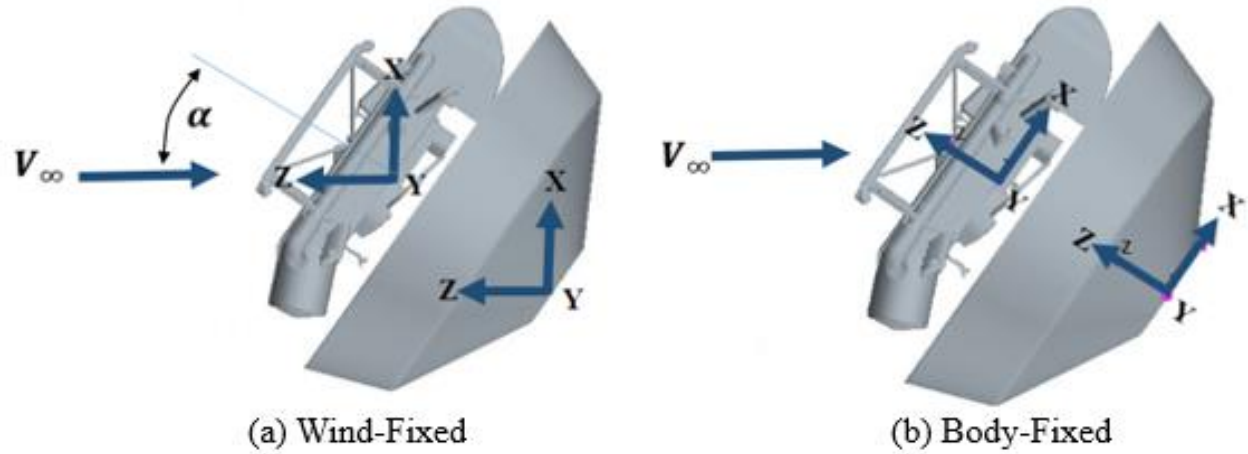

Figure 3: Wind-fixed and body-fixed coordinate frames for Dragonfly's posed configuration

There exists a difficulty in conducting experimental testing on Earth stemming from the inability to accurately replicate the atmospheric conditions of Mars and Titan in terms of scaling. As a result, efforts across all international agencies have resulted in a 40 percent success rate of missions to Mars, emphasizing the necessity for alternative testing methods [7]. Frequent geometric and mechanical design changes during the development phase also pose a significant challenge to physical testing. One alternative approach is the application of computational fluid dynamic (CFD) modeling, which has the capability to modify and simplify geometries, accurately

replicate atmospheric and physical conditions, and eliminate the need to reserve physical testing facilities. Presented here are studies that evaluate the aerodynamics of the Dragonfly lander-backshell system during Preparation for Powered Flight (PPF), as depicted in Figure 1. The methodology, coordinate frames, and mesh sensitivity studies used are discussed extensively in Chapter 2. In support of the CFD approach taken, various unit-test benchmarks were completed for Dragonfly's lander-backshell system and compared with published experimental data for the Mars Exploration Rover (MER), Ahmed body (lander-like bodies), and Robin body (rotor-lander interaction) to develop confidence in the CFD numerical model [8]–[13]. Additional validation for modeling rigid coaxial rotors using Blade Element Method (BEM) was conducted by Penn State University, which reduces the overall computational cost of current and future research efforts [14]. Unit-test benchmarks comparing CFD results against experimental data provide a method of quantifying uncertainty between the StarCCM+ computational solver and the experimental results, and provides reasoning to the methodology presented in this research. Following benchmark analysis, CFD simulations supporting Dragonfly's descent on Titan were developed to analyze the aerodynamic character of the lander-backshell system in PPF, specifically targeting the impact of lander-backshell and rotor-body interactions to provide solutions for achieving positive control authority for successful despin.

CHAPTER 2: METHODS

2.1 CFD Model Formulation

The primary objective of these studies was to observe the complex aerodynamics experienced in atmospheric descent at low altitudes using StarCCM+, a commercially available CFD software. The computational model implemented SIMPLE for its segregated flow solver, a numerical algorithm which couples the pressure and velocity through a pressure correction equation to satisfy the velocity field via mass conservation [15]. This predictor-correction method is sufficient for constant density, low Mach number flows, similar to the types of scenarios investigated in this EDL research. Spalart-Allmaras turbulence modeling was applied under the assumption of constant density for the numerical model, given the lander's low altitude in Titan's atmosphere. The four coaxial rotor blades of Dragonfly were modeled using time-averaged blade element momentum (BEM) theory, as outlined in Figure 4. BEM was coupled with the aforementioned CFD algorithms to solve Navier-Stokes equations without requiring precise rotor blade geometries. The computations were carried out by selecting cells within the computational domain, specifying geometrical dimensions and orientations, and defining the size of the two-dimensional interpolation grid. The momentum source term was evaluated for each blade element on this interpolation grid and associated to a set of cells within the volume mesh, then drawing information from the nearest cell to the blade element. As a result, the computational effort was highly dependent on the grid size [15].

Unit-test benchmark studies were conducted to compare the accuracy of the CFD approach to experimental data sets. Surface pressure data and aerodynamic coefficients including lift, drag, and pitch moment were computed and validated against published test data [8]. The benchmark

simulations were first completed using a Reynolds Averaged Navier Stokes (RANS) model, in which the Navier-Stokes equations were decomposed into mean values and perturbations, or fluctuations about the mean value. This time-averaging technique is usually employed in steady-state situations. The scenarios were simulated again using an unsteady Reynolds Averaged Navier Stokes (URANS) model and were compared to the same experimental data sets. The URANS equations include additional temporal derivatives of the velocity terms which are computed across the desired number of time steps. Before completing a URANS simulation, the faster and less robust RANS model was implemented to initialize to a converged starting solution prior to running the time-accurate solver. Timesteps for the URANS simulations were determined by maintaining a Courant number near unity. The governing equations of the Eulerian model incorporate principles of mass, momentum, and turbulence modeling. The gas flow equations for mass and momentum balance during descent into Titan's atmosphere are, respectively

$$\nabla \cdot \bar{v} = 0 \tag{1}$$

$$\rho \frac{\partial}{\partial t}(\bar{v}) + \rho \nabla \cdot (\bar{v} \otimes \bar{v}) = -\nabla \cdot \bar{p}\mathbf{I} + \nabla \cdot (\overline{\mathbf{T}} + \mathbf{T}_{RANS}) + f_b \tag{2}$$

$$\frac{\partial}{\partial t}(\rho \tilde{v}) + \nabla \cdot (\rho \tilde{v} \overline{\boldsymbol{v}}) = \frac{1}{\sigma_{\tilde{v}}} \nabla \cdot [(\mu + \rho \tilde{v}) \nabla \tilde{v}] + P_{\tilde{v}} + S_{\tilde{v}} \tag{3}$$

$$\sum_f \dot{m}_f = \sum_f (\dot{m}^*{}_f + \dot{m}'{}_f) = 0 \tag{4}$$

$$p^{n+1} = p^n + \omega p' \tag{5}$$

$$\dot{m}_f{}^{n+1} = \dot{m}^*{}_f + \dot{m}'{}_f \tag{6}$$

$$v_p^{n+1} = v_p^* - \frac{V \nabla p^*}{a' {}_p^v} \tag{7}$$

Equation 1 shows the continuity equation which must be solved to satisfy conservation of mass. Equation 2 displays the conservation of momentum equation. Eliminating the transient temporal term returns the RANS form of the momentum equation. Equation 3 presents the standard low-Reynolds number Spalart-Allmaras turbulence model which calculates the turbulent eddy viscosity by solving the modified diffusivity, $\tilde{\nu}$. The model resolves both the turbulent boundary layer and the viscous sublayer via the standard transport equation. The increased use of the Spalart-Allmaras turbulence model in aerospace applications can be attributed to its simplified integration into unstructured CFD solvers. To account for the details of rotor aerodynamics, a source term f_b is introduced to Equation 3. The time-averaged RANS model filters out the fluctuating transient terms from the Navier-Stokes equations. Equation 4 through Equation 7 show the pressure-correction equation and the corresponding variable updates within the SIMPLE algorithm procedure. The breakdown of the computational mesh, indicated in red, and the discretized blade element in both the azimuthal and radial directions are shown in Figure 4. The blade element structure lays the foundation for the inflow model that is used in both benchmark analysis and the Dragonfly PPF simulations.

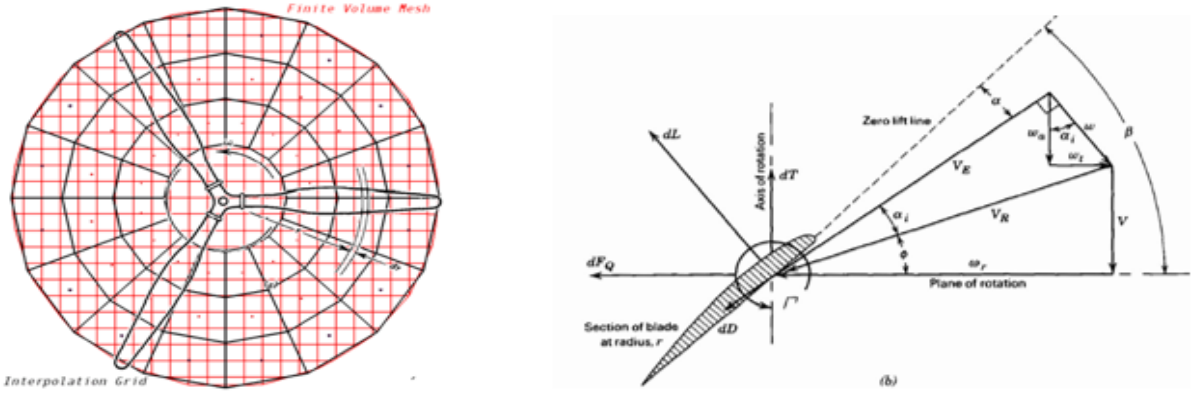

(a) Computational and rotor BEM mesh (b) Corresponding velocity configuration

Figure 4: Blade discretization and virtual disk representation of a rotor [13]

2.2 Benchmark Analysis

The MER backshell and Ahmed body function as representative geometries for Dragonfly's backshell and lander body, respectively, and seek to imitate the aerodynamic behavior observed during Dragonfly's free-stream descent. To bolster the reliability of the numerical solver's ability to reproduce experimental results, a number of benchmark assessments were performed. The purpose of these studies was to reduce uncertainty in the overall CFD approach and numerical models to establish a foundation to develop a simulation framework for Dragonfly. Prior to Dragonfly EDL simulations, three benchmark studies were conducted. These included evaluations of the MER backshell, Ahmed body, and Robin body interactions. A mesh refinement procedure was followed for each individual benchmark analysis to ensure the results obtained from CFD were not impacted by the developed mesh. Mesh independence was achieved by attaining an infinite case solution, or the solution for a negligibly small mesh size, and selecting a cell reference size from the converged region of the solution that effectively balanced the computational run time and discretization error.

2.2.1 Mars Exploration Rover (MER): Backshell Aerodynamics

In the first benchmark study, the MER backshell was modeled in CFD to the specifications outlined in the experimental study [8]. This specific backshell component is of particular interest because it is representative of the backshell geometry used in the Dragonfly EDL sequence. To replicate the open test section conditions of the Vigyan Low Speed Wind Tunnel used in the original experiment, slip walls were modeled on the side boundaries with an inlet velocity of 180 ft/s as shown in Figure 5. The flow is released through a pressure outlet located at the end of the wind tunnel. Figure 6 demonstrates the mesh structure that was used for the MER backshell and

EDL approach, with a conical refinement zone located downstream of the backshell to capture the aerodynamic wake effects in the flow. The backshell was rotated from -10° to 90°, with smaller increments near zero, to simulate the angles of attack that were executed in the original study.

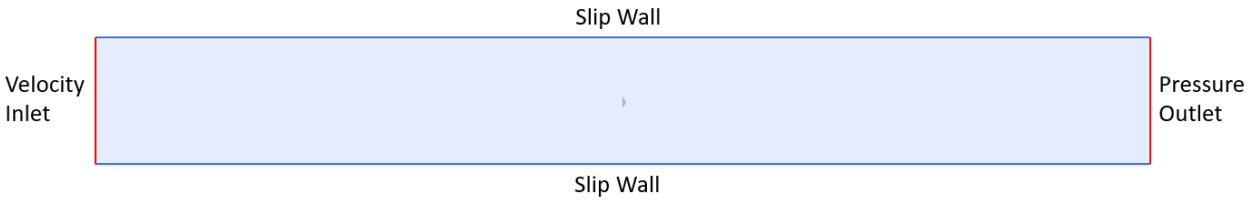

Figure 5: Computational domain for MER simulation

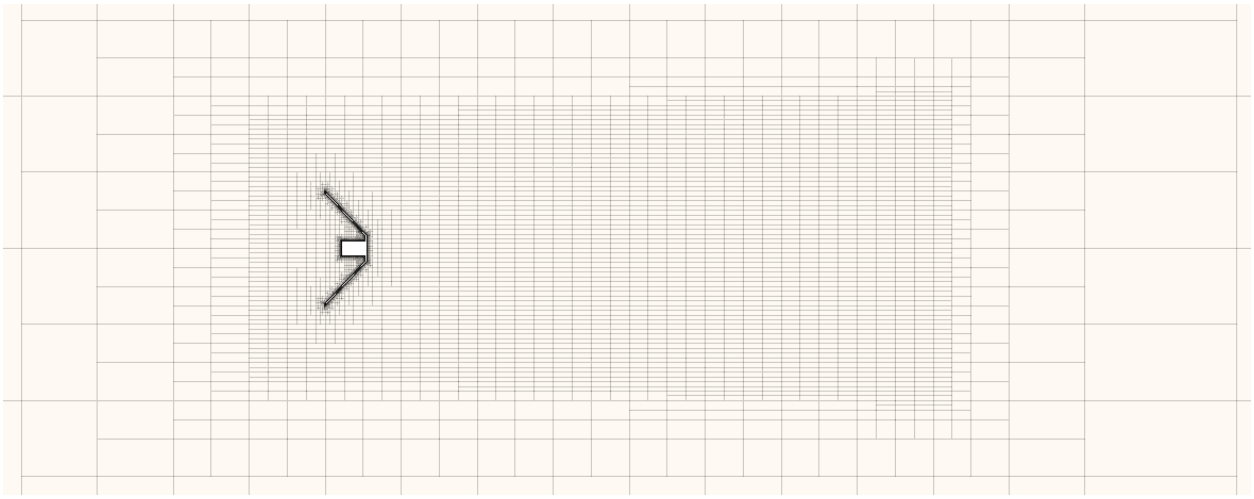

Figure 6: Computational mesh for the MER backshell and domain

Over the designated range of angles of attack, the aerodynamic coefficients of lift, drag, and pitch moment were computed and coplotted against the MER backshell data shown in Figure 7. The CFD solution for the load coefficients used both RANS and URANS models for comparison against the experimental data. The steady and unsteady CFD solution for lift and drag coefficients had a high correlation to the coefficients found in the experiment. The pitch moment coefficient computed using the RANS solver followed the experimental trend in pitch moment coefficient;

however, it contained a slight negative bias. Similarly, the URANS solver followed the experimental trend but slightly underpredicted the pitch moment coefficient. Overall, both the RANS and URANS models were reliable predictors for the trends in the aerodynamic coefficients of backshells in free-stream decent. There was no significant advantages found when using URANS over RANS in this backshell scenario; therefore, quasi-steady models offered significant advantages in terms of computational run time when compared to unsteady models.

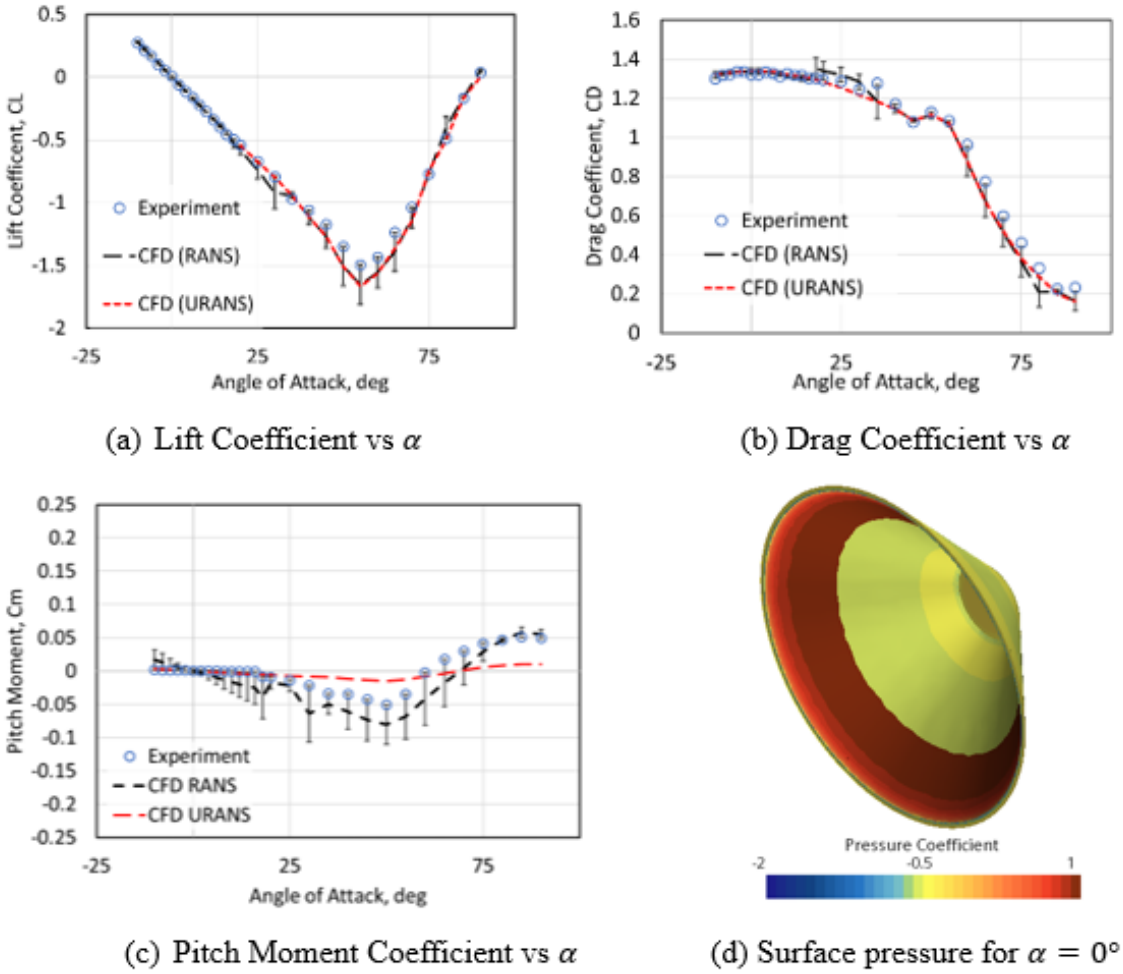

Figure 7: RANS and URANS comparison of aerodynamic coefficients vs angle of attack

To ensure mesh independence prior to benchmark comparison, it was necessary to complete mesh refinement studies. For MER backshell mesh refinement, the lift and drag coefficients were analyzed as a function of mesh size using a least squares regression technique and curve fit. The mesh cell reference size varied from 2.0 to 0.25, where smaller cell sizes were more computationally expensive due to the mesh becoming more refined. The increase in refinement gradually led to a converging solution. Figure 8 shows the coefficient values converging towards the infinite case solution as the mesh approached an infinitesimally small cell reference size. All remaining mesh parameters, such as the conical refinement in the wake, were scaled from the base cell reference size. For the drag coefficient of the MER backshell in free stream descent, the infinite case solution was determined to be 1.334. This solution is unattainable because it represents a theoretical value established by the asymptotically converging fit and suggests that an infinitely refined mesh is achievable. Therefore, a realistic base cell reference size of 0.5 was selected from the converged region. This value sufficiently minimized the computational runtime and mesh discretization error, resulting in a mesh uncertainty of approximately 0.26% when compared to the infinite case drag coefficient.

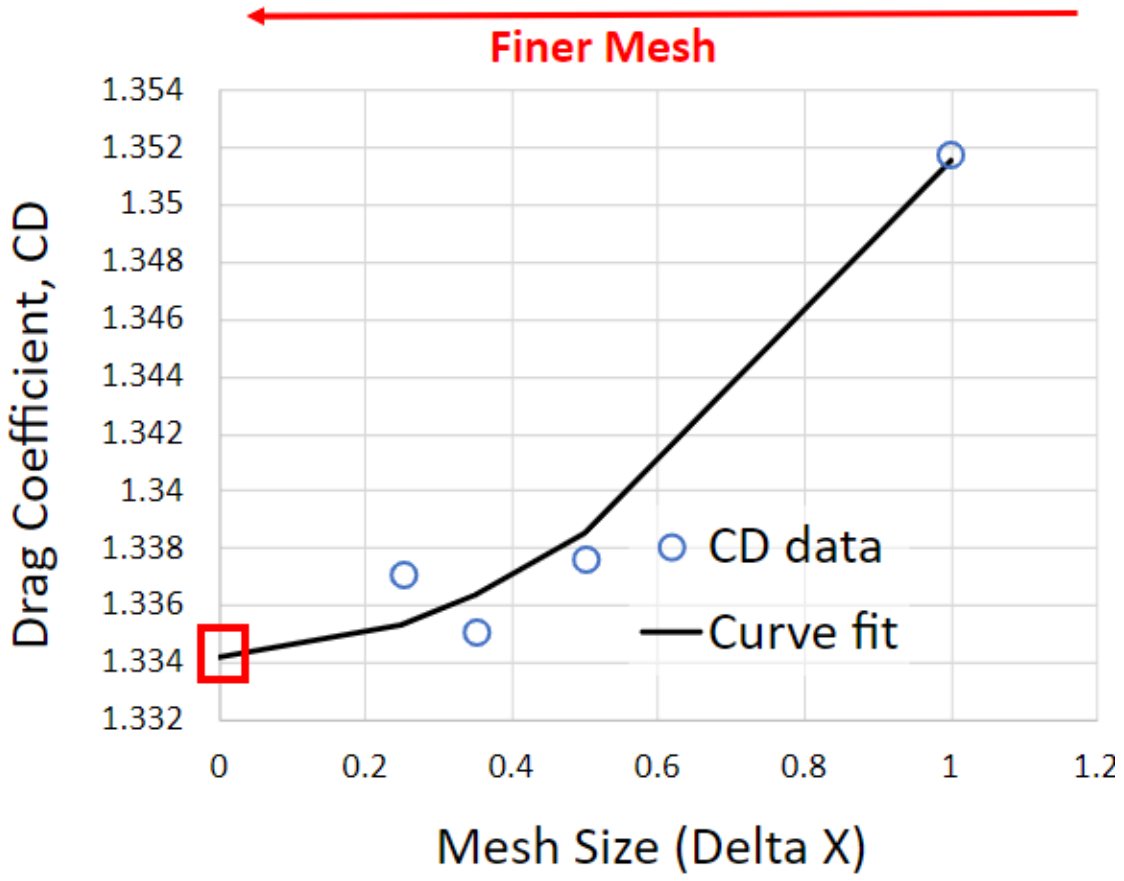

Figure 8: Drag coefficient vs mesh size

2.2.2 Ahmed Body: Dragonfly Fuselage-like Aerodynamics

The Ahmed body is a simplified geometric representation of a car body, commonly used in automotive aerodynamics research. Despite much experimentation throughout the 1970's, it wasn't until 1984 when S.R. Ahmed developed a systematic study which varied the slant angle at the rear of the bluff body that a critical slant angle was identified corresponding to a drastic change in wake structure [16]. The Ahmed body replicates the fluid dynamics typically experienced by a car through flow displacement using a blunt nose, flat sides, and flow separation with a variable geometric rear. Many of the features of the Ahmed body are analogous to the Dragonfly lander body and are a suitable representation of the quadrotor. Reproducing the Ahmed body experiment

using a CFD approach improves the confidence in the software's ability to accurately capture the aerodynamic flow separation and substantiates the selection of RANS, URANS, or detached eddy simulation (DES).

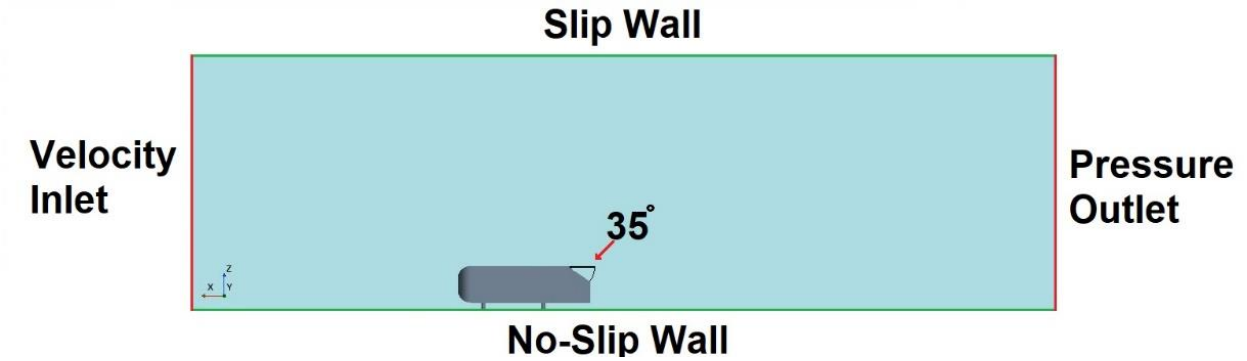

Figure 9: Example Ahmed body geometry

The aim of this benchmark computational study was to vary the sloped angle at the rear of the Ahmed body and observe the changes in flow separation. To align with experimental procedures, simulations were completed for slant angles of 0°, 10°, 20°, and 30°. The computational domain shown in Figure 9 was comprised of three slip walls representing an open environment, a no-slip wall defining ground, a velocity inlet, and a pressure outlet to mimic the open test region in which the original experiment took place. In addition, a blockage ratio was maintained below 1% to match experimental constraints. The time step for the unsteady CFD models was selected to ensure a courant number close to unity.

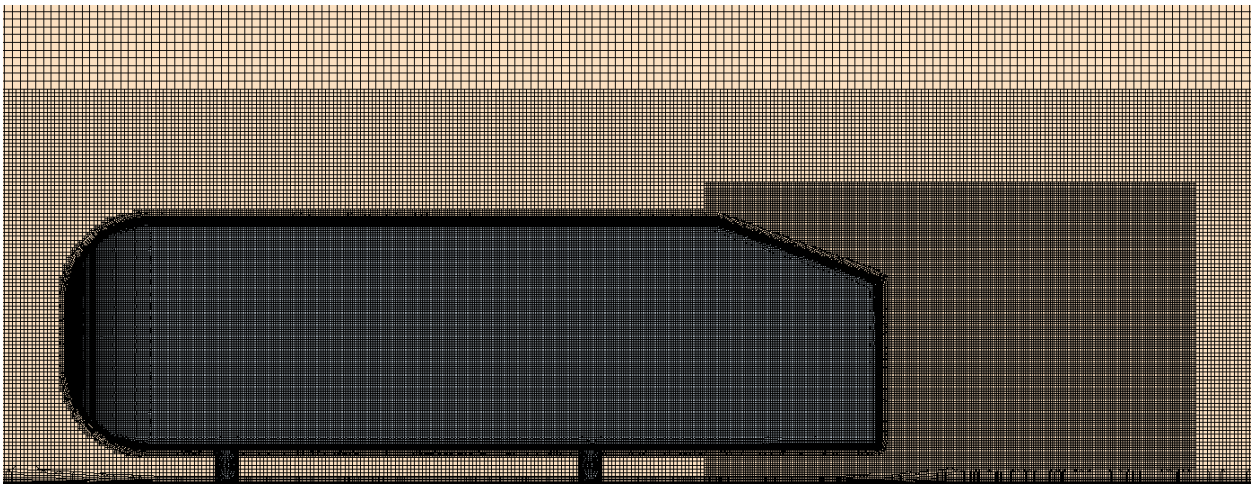

Figure 10: Ahmed body mesh (Wake Size of 2.5mm)

In the initial phase of this benchmark study, a mesh refinement was implemented using RANS. For simplicity, a 2D cross-sectional view of the 3D mesh is illustrated in Figure 10. A more refined region of mesh was implemented just before the slanted rear of the Ahmed body and extended into the bluff-body wake to sufficiently capture the flow character and separation. The mesh in this region is defined as the reference mesh size, or base size. In the remaining near-body regions, the mesh was double the base mesh reference size to reduce the overall computational cost. The base mesh size was varied, and the drag coefficient was calculated as documented in Figure 11. Following the same procedure outlined in Benchmark 1, a final cell reference size of 2.5*mm* was selected.

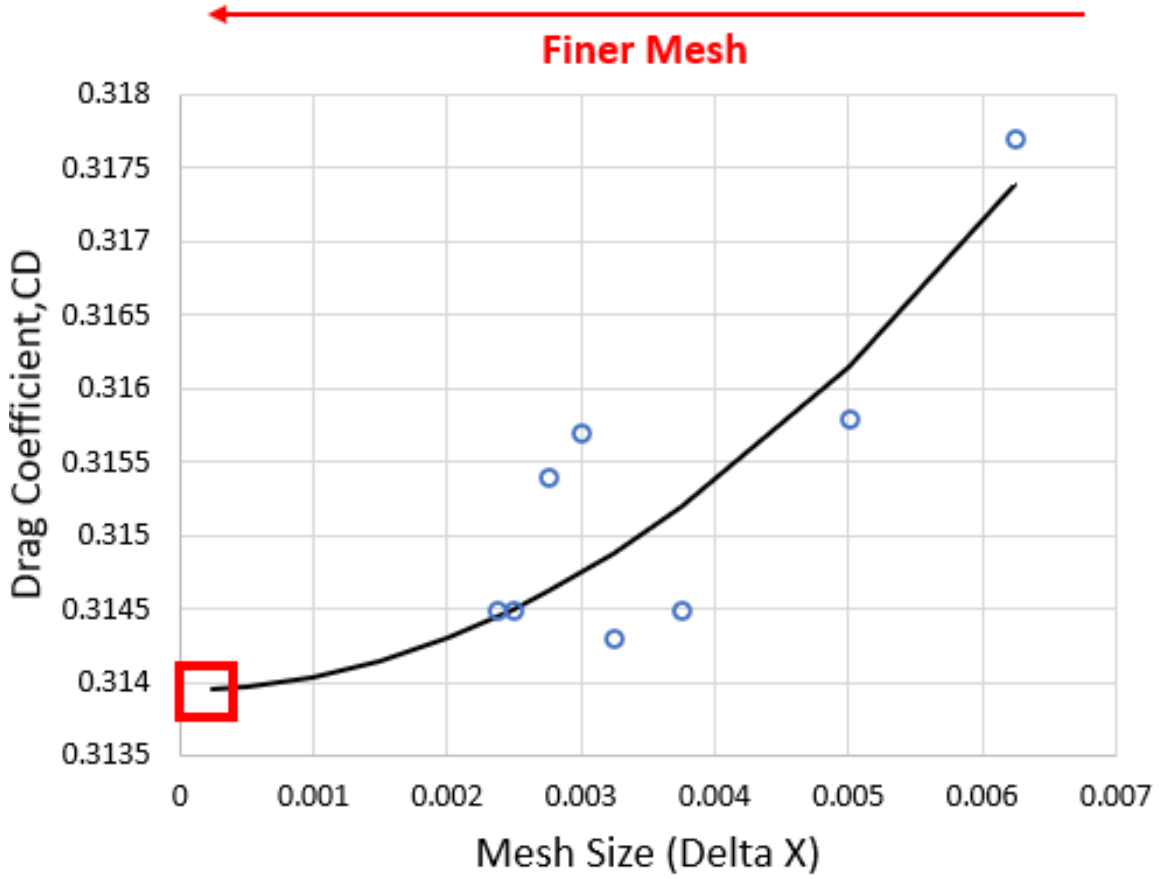

Figure 11: Drag coefficient vs mesh size

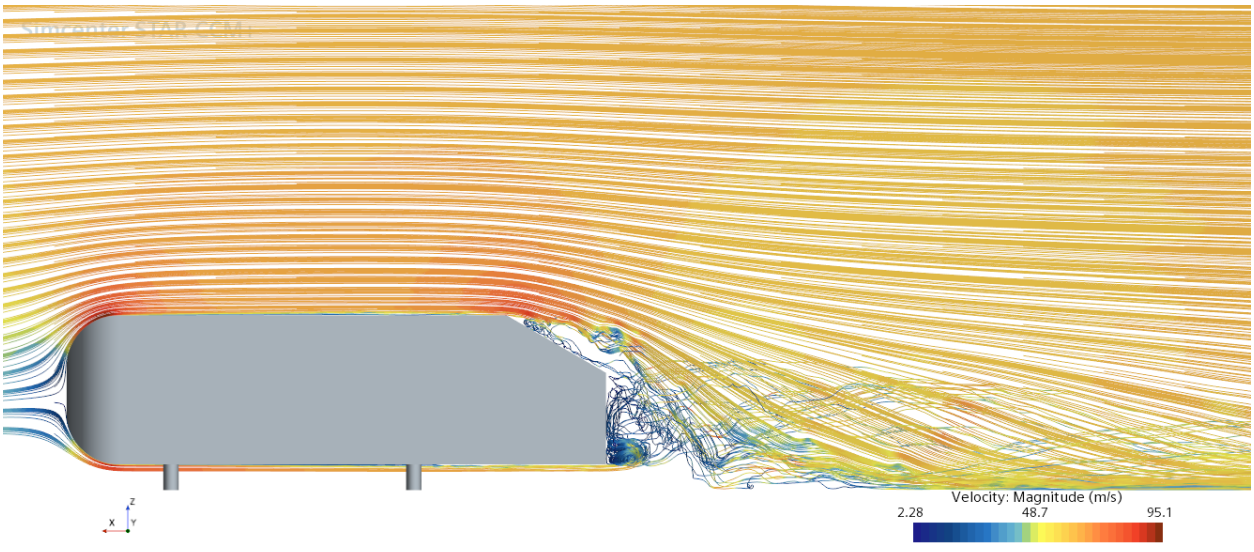

Figure 12: Streamlines of 30-degree slant Ahmed body using DES modeling

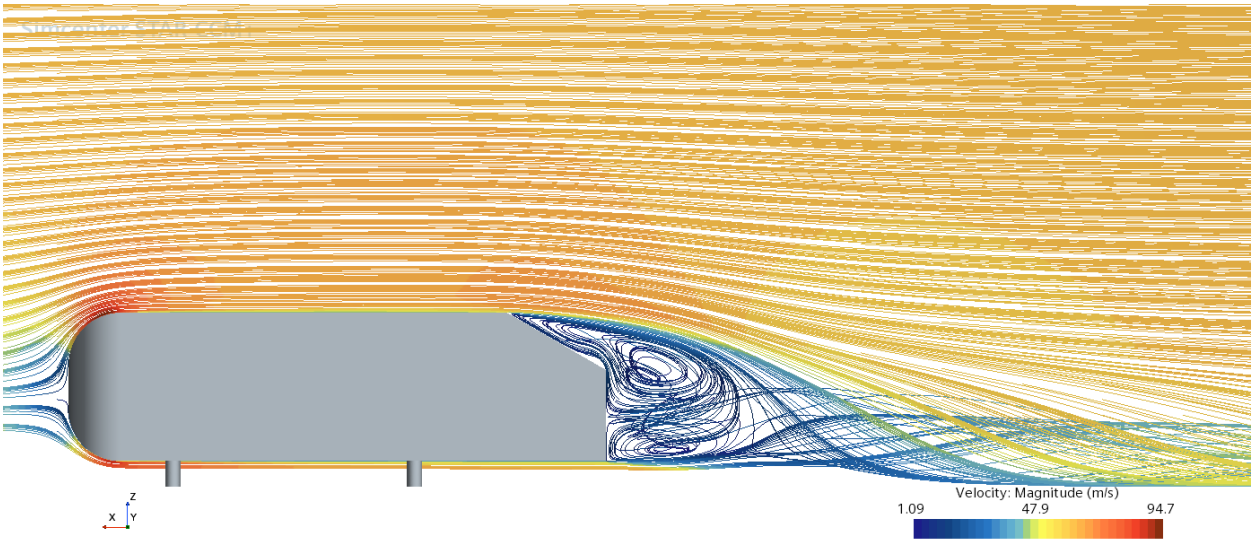

Figure 13: Streamlines of 30-degree slant Ahmed body using URANS modeling

Despite each physics model having a comparable bias, all models were able to replicate the trend in drag behavior with respect to the changing slant angle. These findings aligned well with other research using the Ahmed body, which concluded the Spalart-Allmaras turbulence model tended to overpredict drag [10]. From the experiments of S.R. Ahmed and the research that followed, it became well known that 30° was the critical slant angle in which a drastic change in wake structure would be experienced behind the bluff body. At this point, the flow could either remain attached or fully separate from the slanted section resulting in varying drag coefficient values [9]. The 30° critical slant angle case was the only simulation where the numerical models showed a significant difference when compared to one another. At this critical slant angle, the RANS model failed to capture the turbulent kinetic energy in the flow, making it challenging to observe the subtle flow attachment on the slanted surface. As a result, there was insufficient energy to prevent flow separation from the surface [11]. Alternatively, the DES model had the best performance in accurately capturing the drag. With knowledge of the Dragonfly lander geometry, and the ability to design additional kitting for the quadrotor, the RANS model was selected for

generating and simulating larger data sets. The steady model was accurate over a large enough range of slant angles before the critical transition point to be used in studying the aerodynamic flow character over Dragonfly's lander body. URANS and DES were not selected as the principal model for Dragonfly simulations due to their high computational cost; however, the URANS model was used sparingly to validate the generated RANS data.

2.2.3 Rotor Aerodynamics: Rotor-Aerodynamic Assessments

In addition to benchmark comparisons for the backshell and lander body, it was important to analyze how CFD captured rotor-body interaction. A third benchmark study was completed to assess the accuracy of the CFD solution in simulating the behavior of a 4-bladed rotor near a ROBIN (ROtor Body INteraction) body, representative of a common helicopter. Using the experimental setup from reference [13], steady state surface pressures and load information were measured at varying advance ratios and thrust coefficients (Ct). The experimental setup and CFD flow field visualizations are provided in Figure 14 and Figure 15. The simulations were effective in capturing the overall flow behavior along the fuselage and the surface pressure coefficients along the fuselage centerline agreed well with the experimental results. Higher advance ratios posed a greater difficulty in simulating the surface pressures in the wake region located aft of mid-fuselage, which made it difficult to compute aerodynamic loads at this location. It is important to note, the ROBIN configuration consists of a single rotor placed directly above the body, whereas Dragonfly is a quadrotor vehicle with coaxial rotors offset in a typical quadrotor drone setup. The interactions and surface pressures between Dragonfly's rotors and the Dragonfly lander may differ significantly from those of the ROBIN body; however, this benchmark analysis supports the CFD software's ability to accurately capture the resulting surface pressures.

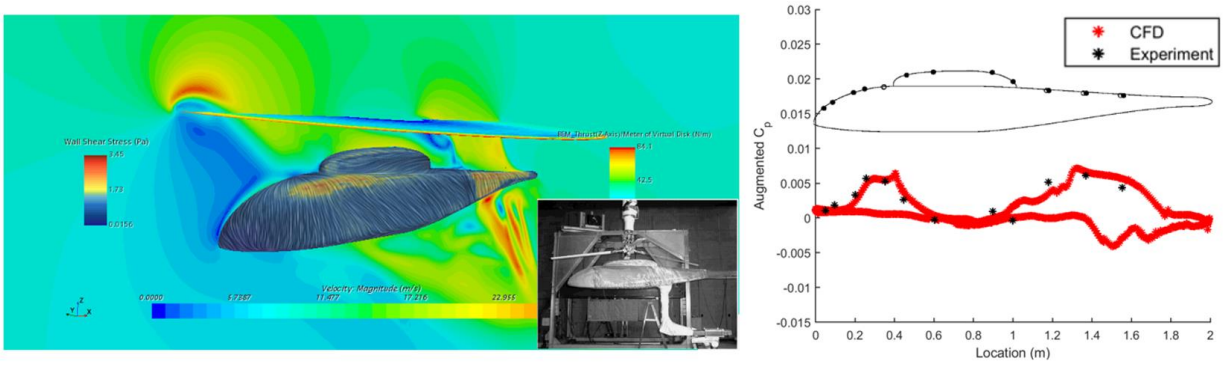

Figure 14: Flow field visualization and surface pressure coefficient of Robin body
(Advance ratio = .05 & Ct = .0064)

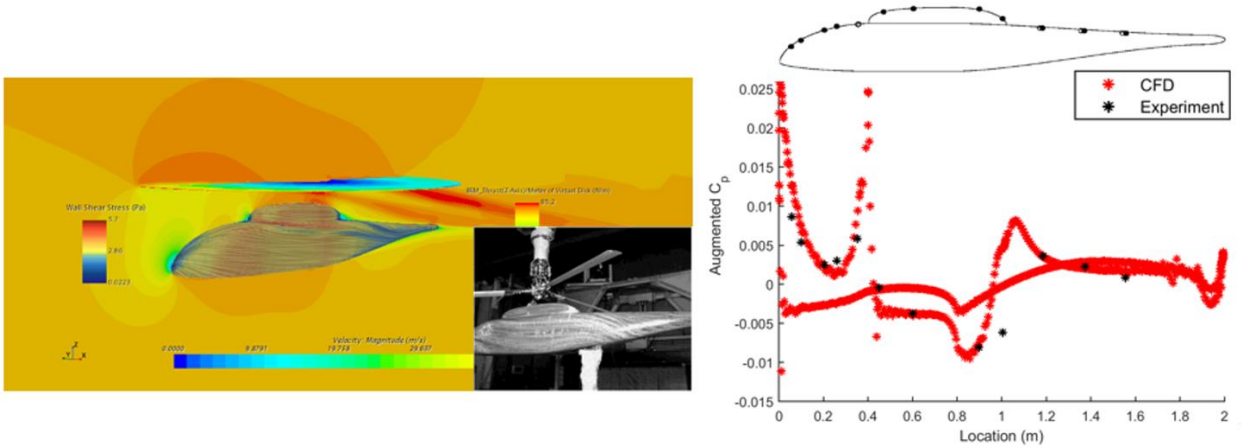

Figure 15: Flow field visualization and surface pressure coefficient of Robin body
(Advance ratio = .23 & Ct = .0064)

2.3 Computational Domain: Dragonfly

Figure 16 outlines the computational domain used for Dragonfly PPF descent. The scale of the domain was derived from a general length scale, which was assumed to be the diameter of Dragonfly's backshell (e.g., L ≈ 4.5m). The domain extended out from the lander-backshell system in all directions approximately 30m to provide sufficient volume for capturing relevant aerodynamic effects. Baseline simulations were modified to incorporate Dragonfly's current lander geometry, backshell, and kitting in varying descent scenarios, only after ensuring the accuracy and

reliability of the CFD approach through benchmark analysis. The objective for each CFD simulation was to observe the flow character around Dragonfly's lander-backshell system and compute the loads and moments associated with the specific descent scenario. A major focus within each study was to determine the impact of the aerodynamic loading on yaw rotation, or Z-moment, which was critical in determining if successful despin was achieved. The first two studies were aimed at defining whether Dragonfly's backshell had any significant influence on the rotor generated suction force or the system's ability to successfully despin. Dragonfly's backshell plays a small role in terms of time used within the mission timeline and could offer the simplest fix if results showed a benefit to the despin moment. The remaining studies focused on rotor control using different RPM speed settings, in addition to altering the rotor cant. The PPF descent simulations employed RANS modeling with a BEM solver as described previously in model formulation but implemented a free-stream velocity of $3.25 m/s$. The computational Dragonfly model used a 3D triangular surface mesher with a trimmed cell mesher applied throughout the domain for volume meshing. A prism layer mesh was coupled with the core volume mesh to generate prismatic cells near the lander and backshell walls to refine the accuracy of the flow solution at the boundary. Like the MER backshell mesh, a 3D conical refinement zone was included to enhance the solution accuracy in the wake, as displayed in Figure 17. Additional mesh parameters and cell-reference sizing is included in Table 1.

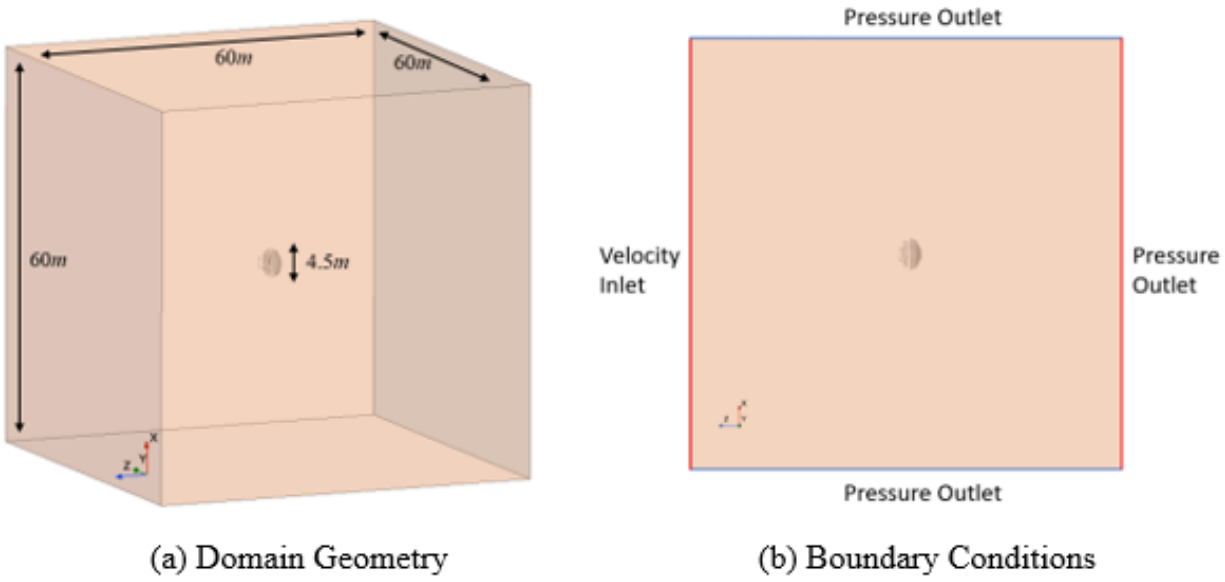

Figure 16: Computational domain of Dragonfly in free stream descent

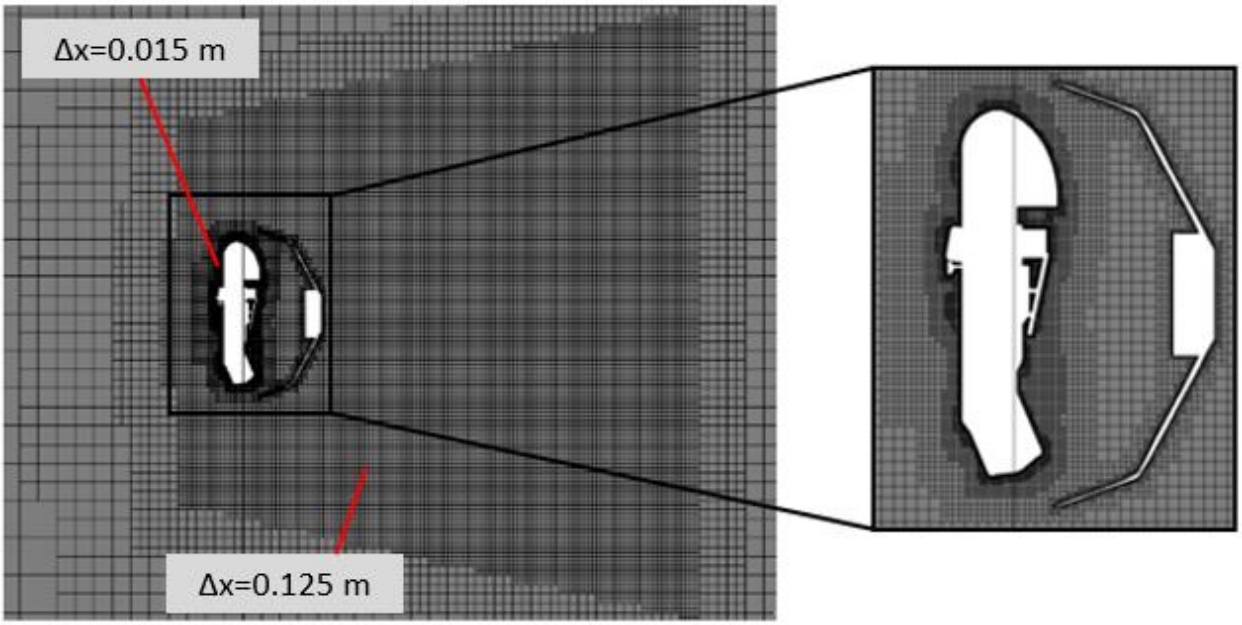

Figure 17: Volume mesh with conical wake refinement zone

Table 1: Summary of computational mesh parameters

MESH PROPERTY	VALUE
NUMBER OF CELLS	**20 x 10^6**
NEAR BODY SPACING, $\frac{\Delta x_{nb}}{L}$	**0.003*m***
WAKE SPACING, $\frac{\Delta x_w}{L}$	**0.027*m***
LANDER SPACING, $\frac{\Delta x_l}{L}$	**0.014*m***
BACKSHELL SPACING, $\frac{\Delta x_{bs}}{L}$	**0.014*m***
LANDER WALL, y^+	**1-15***
BACKSHELL WALL, y^+	**1-15***

*Note, using all y^+ wall function

CHAPTER 3: RESULTS AND DISCUSSIONS

3.1 Backshell Independence

Dragonfly's backshell plays a major role in EDL and is the primary structural link between the main parachute and lander body. The backshell completes its service following lander release from its guiderails directly into powered flight. At this point, the backshell is no longer required and has no further impact on the remaining mission; therefore, design changes relating to the backshell would have little impact on forward flight and Dragonfly exploration. Implementation of new backshell designs and backshell descent methods would offer the easiest solution to despin in terms of application and impact on future mission success, if the results showed a beneficial impact on the suction torque and rotor control authority.

3.1.1 Backshell Venting

Dragonfly's current backshell configuration contains one hole as shown in Figure 18, along with three alternative venting options. The purpose of this trade study was to analyze how the addition or subtraction of holes, or venting, would influence the systems X, Y, and Z moments. For reference, the coordinate axes and rotor definitions are outlined in Figure 19. In the EDL coordinate frame, referenced in Figure 3, the moment about the Z-axis is defined as the despin moment. Analysis of moment trends over a range of angles of attack and side slips was conducted to determine if there was any added benefit to system stability from backshell venting. From preliminary analysis, no correlation was observed between the despin moment on the system and the backshell configurations when subject to varying angles of attack and side slips. The suction torque and despin moment were found to be independent of all backshell venting configurations.

Consequently, the research in this study was directed towards examining the impact of different backshell configurations solely on the X-moment as a function of side slip, and the Y-moment as a function of angle of attack. Dragonfly is descending during PPF, so it is important to note the yaw direction in the EDL configuration is different from forward flight. Unlike forward flight, EDL has a yaw rotation about the X-axis with the incoming free stream velocity in the negative Z direction, as shown in Figure 19.

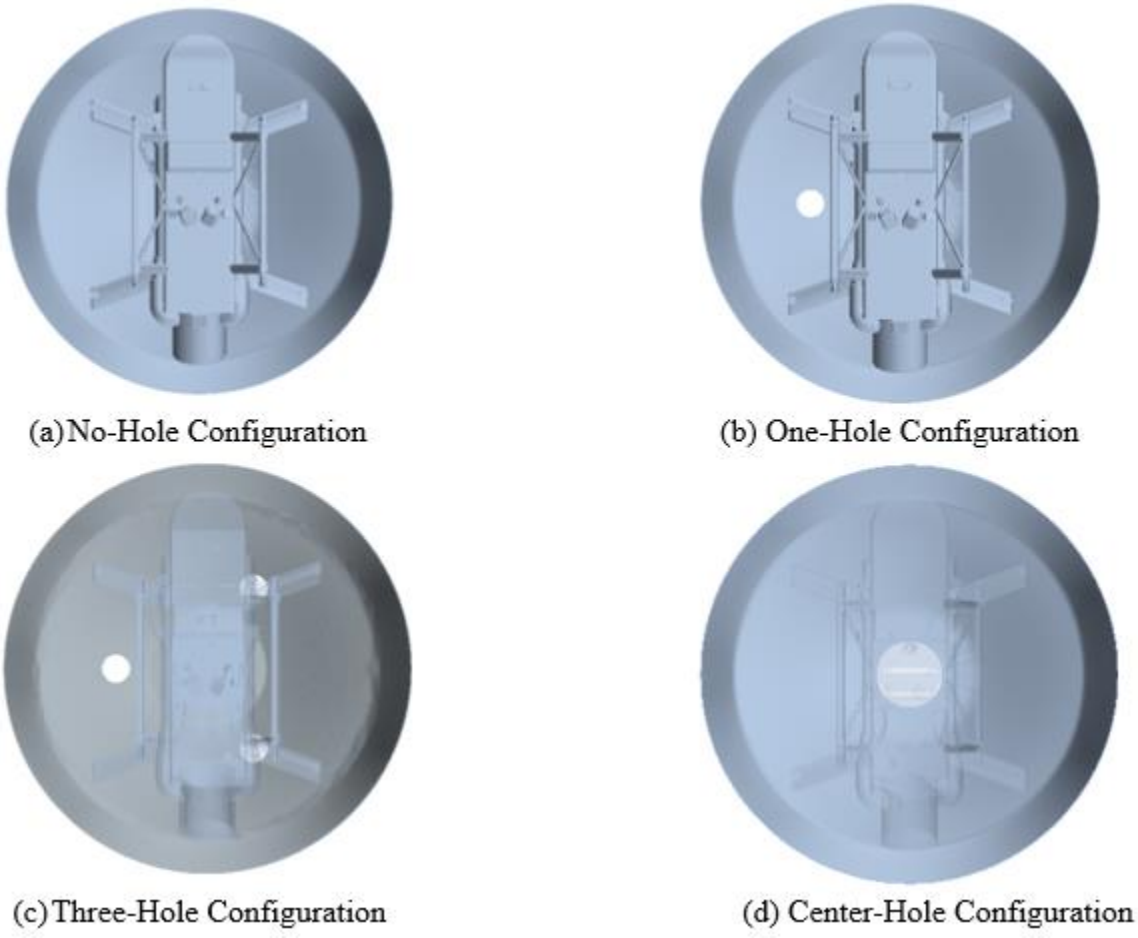

Figure 18: Hole configurations for vent study

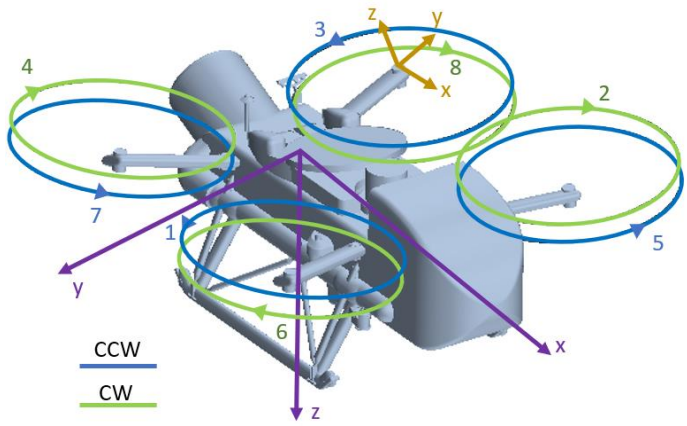

Figure 19: Dragonfly rotor configuration with body-fixed reference frame and rotor-fixed reference frame

With respect to quadrotor dynamics, the X-moment of the system exhibited a considerable dependence on the side slip angle (X-axis rotation), and the Y-moment was heavily reliant on the induced angle of attack (Y-axis rotation). Therefore, the moments were plotted against their respective angles of influence. Figure 20 illustrates the positive sign conventions for side slip and angle of attack for Dragonfly in a free stream descent. In this diagram a negative X-moment is required to restore a positive applied side slip angle and a positive X-moment is required to restore a negative applied side slip angle. Similarly, a negative applied Y-moment is required to restore a positive applied angle of attack and a positive Y-moment is required to restore a negative applied angle of attack.

The backshell vent trade study was conducted using negative induced side slip angles; therefore, a positive X-moment was required to restore the system to its original zero degree starting orientation to remain stable. Figure 21(a) displays the overall X-moment as a function of side slip for the no-hole, one-hole, three-hole, and center “parachute” hole configurations. The moments are reported in the wind-fixed non-rotating reference frame. Beginning at negative 20-degrees side slip, all backshell configurations experienced a positive X-moment which opposed

the induced negative side slip angle. In other words, the system opposed the rotation of the induced side slip and generated a moment in the direction of the original starting orientation. This result led to a stable system. Between negative 20-degrees and negative 5-degrees, the no-hole and three-hole backshell configurations increased in slope, representing a local instability. In this region, the restoration moment decreased as side slip became increasingly negative; however, this decrease in restoration moment was relatively small in scale (on the order of 1 Newton). The local instability had minimal effect and both configurations maintained an overall restoring moment as indicated by the X-moment remaining positive. Thus, there was not sufficient justification for modifying the existing backshell design because the magnitude changes of the X-moment between negative 20-degrees and negative 5-degrees was negligible and the overall system remained stable. Alternatively, the results for the 0-degree case, or no induced side slip, favored the symmetric venting of the no-hole and center-hole configurations. To remain passively stable about the X-axis, Dragonfly must experience little to no moment at 0-degree side slip. Here, the asymmetric backshell configurations experienced larger moments when compared to the symmetric configurations, resulting in unwanted system rotation out of straight descent. As predicted, the asymmetric hole placement resulted in a moment generation with no induced side slip.

Figure 21(b) shows the Y-moment as a function of induced pitch, where the backshell configuration with no hole obtained the highest restoring moment at a negative 20-degree angle of attack. In addition, the no-hole and center-hole configurations observed the lowest total moments at zero angle of attack. At smaller induced angles, the asymmetric one-hole and three-hole configurations experienced a negative Y-moment, which meant Dragonfly continued to rotate in the negative direction. This resulted in an unstable system at low angles of attack. Although the magnitudes of these moments were relatively small, the asymmetric vent positions showed another

unstable effect on aerodynamic character. Figure 22 displays the velocity contour plots that were developed to visualize the influence of each vent configuration on the flow character around Dragonfly. Overall, the symmetric backshell designs were more favorable when compared to the asymmetric configurations, which experienced a greater degree of unsteady behavior and undesired moments in the absence of an induced angle of attack. Despite finding no configuration capable of resolving the issue of despin, this investigation did reveal that modification of the current one-hole backshell design could see potential improvement if changed to a symmetric hole placement. More importantly, backshell vent placement was found to be independent of despin moment and had little impact on control authority.

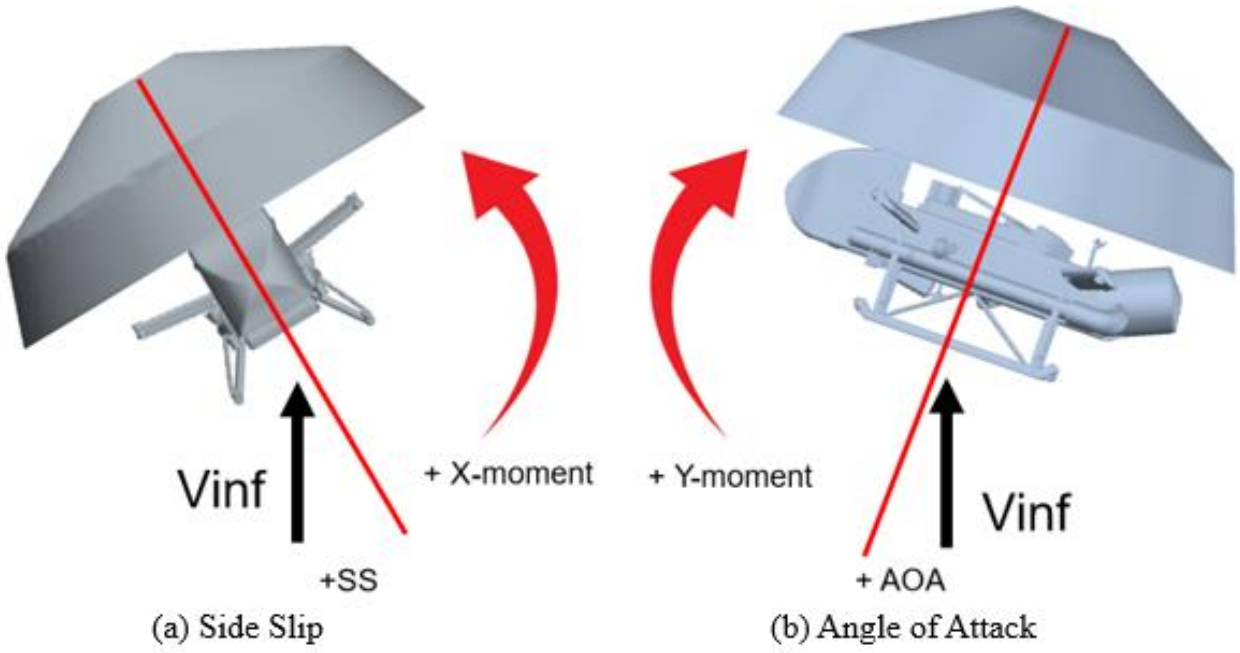

Figure 20: Positive sign conventions for side slip and angle of attack

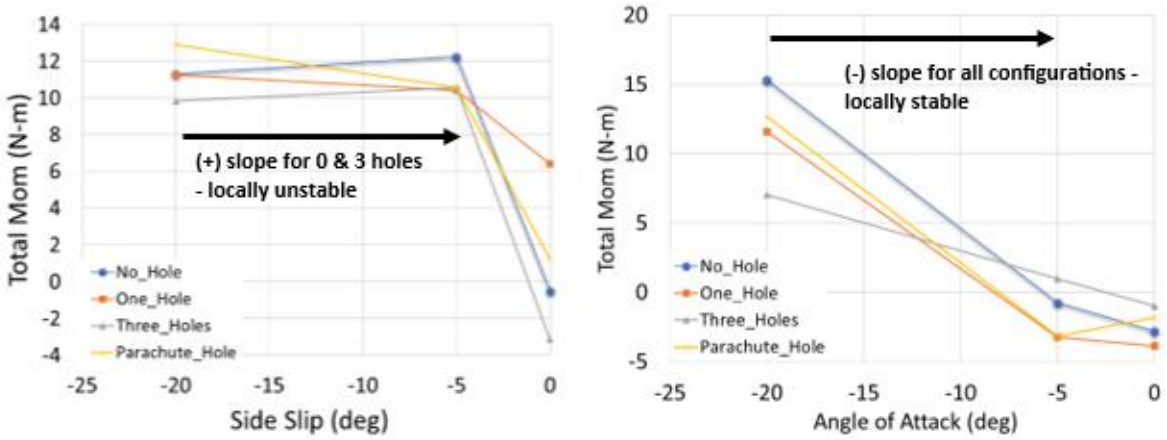

Figure 21: Total moment for each backshell configuration vs induced side slip and angle of attack, respectively

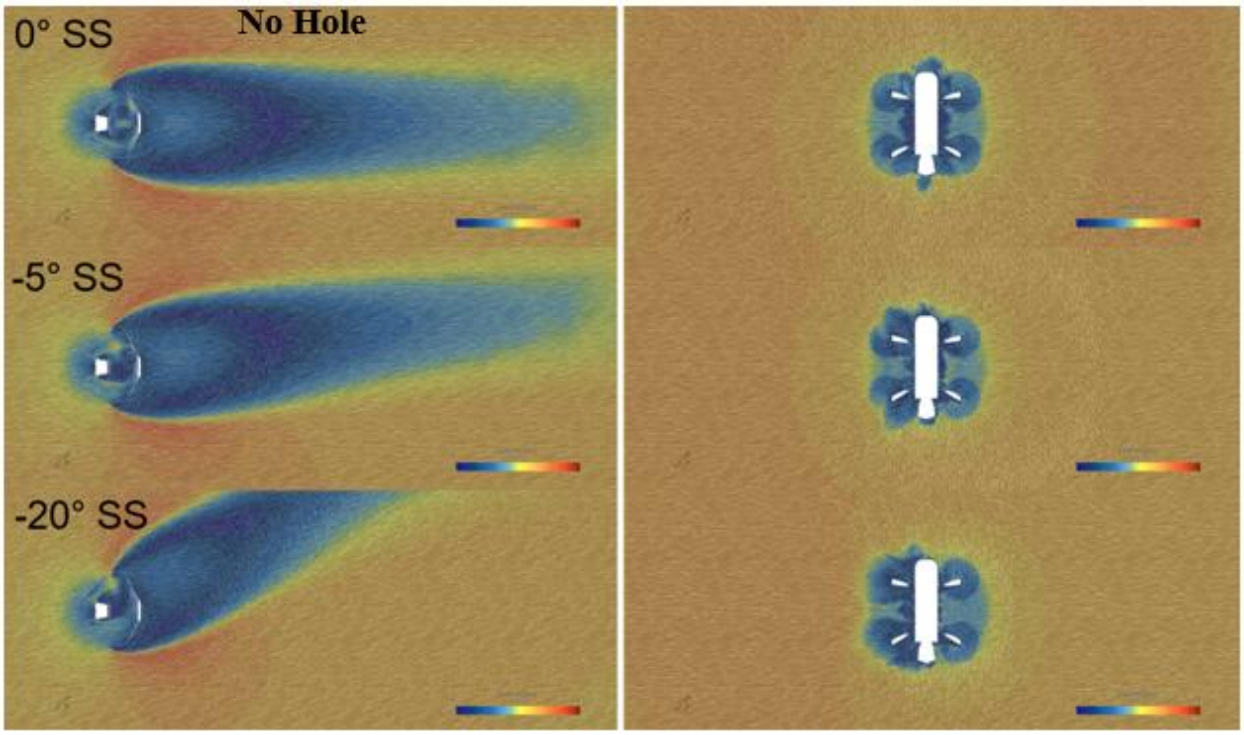

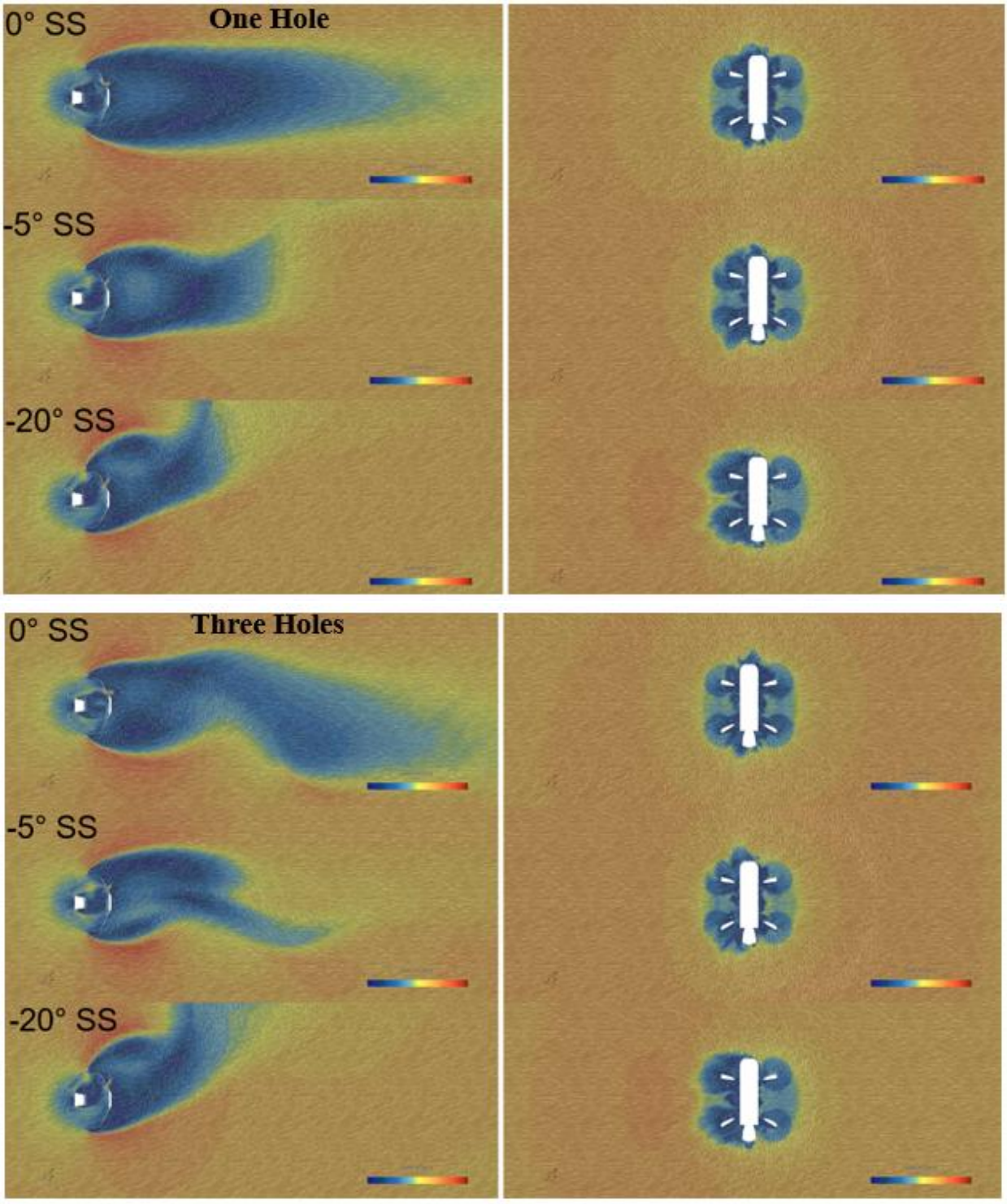
0° SS
One Hole
-5° SS
-20° SS
0° SS
Three Holes
-5° SS
-20° SS

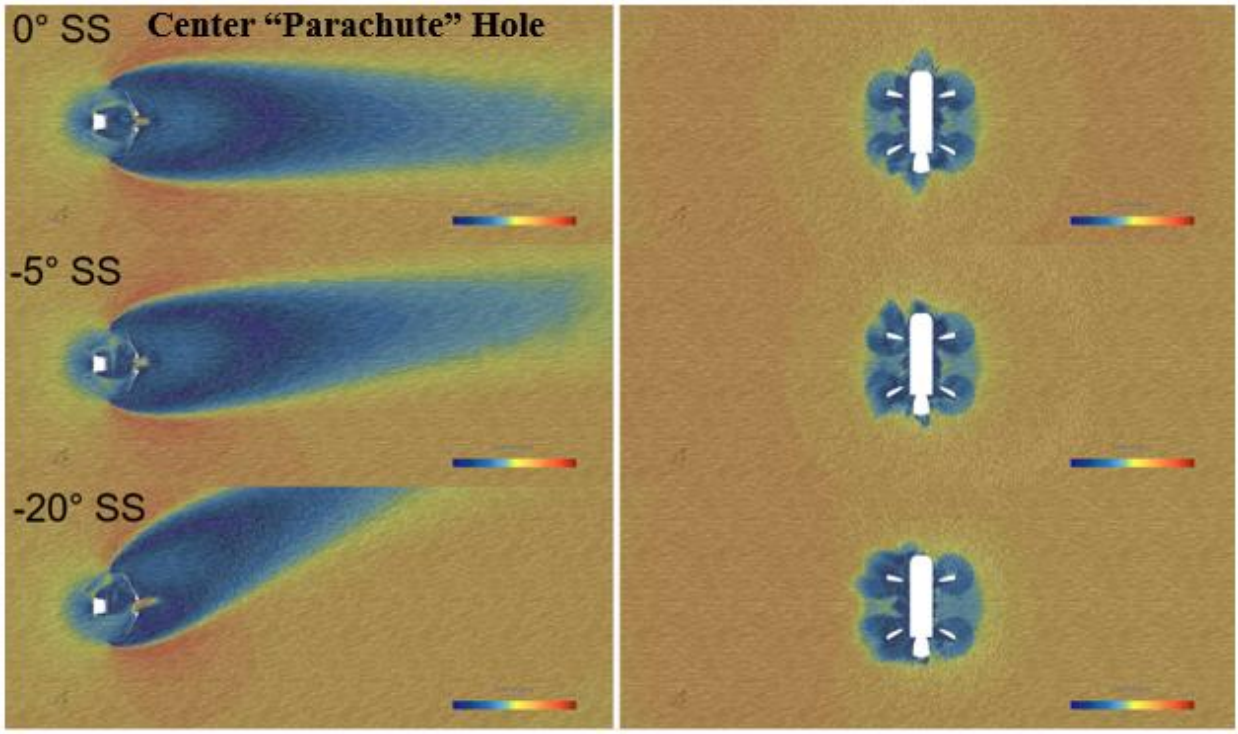

Figure 22: Velocity flow field visualizations for each backshell configuration as a function of side slip angle

Visualizing the distribution of pressure coefficients along the backshell provides a higher-level understanding of the restoring moments. Discretization of the backshell into X and Y planes enabled the calculation of pressure coefficients at each Y-position and X-position, respectively. Specifically, discretizing the backshell into X planes provided clear trends in yaw moment about the x-axis generated by the induced side slip. For clarity, only the pressure coefficients along a single X plane are presented for the three side slip angles [X = -0.5m]. These plots are shown in Figure 23. Positive Y-position values represent the starboard side of the lander body and negative Y-positions indicate the port side of the lander body. All backshell configurations displayed a larger gap at negative Y-positions indicating a greater pressure difference on the port side of the lander. This led to the generation of a restoring moment resulting in a starboard rotation. The peaks observed near the ends of the plots are representative of changing backshell geometry and are

attributed to the backshell's corners. At higher side slip angles, the magnitude difference in the restoring moment between backshell configurations did not substantiate a modification to the current backshell design. Continued research using symmetric hole configurations may provide more clarity on the potential advantages for pitch and roll stability attributed to the system X and Y moments. As previously stated, venting the backshell was found to be independent of the suction torque and despin moment. This development led to the question whether Dragonfly's backshell had any influence at all on the suction force and system despin, which is addressed in the following study.

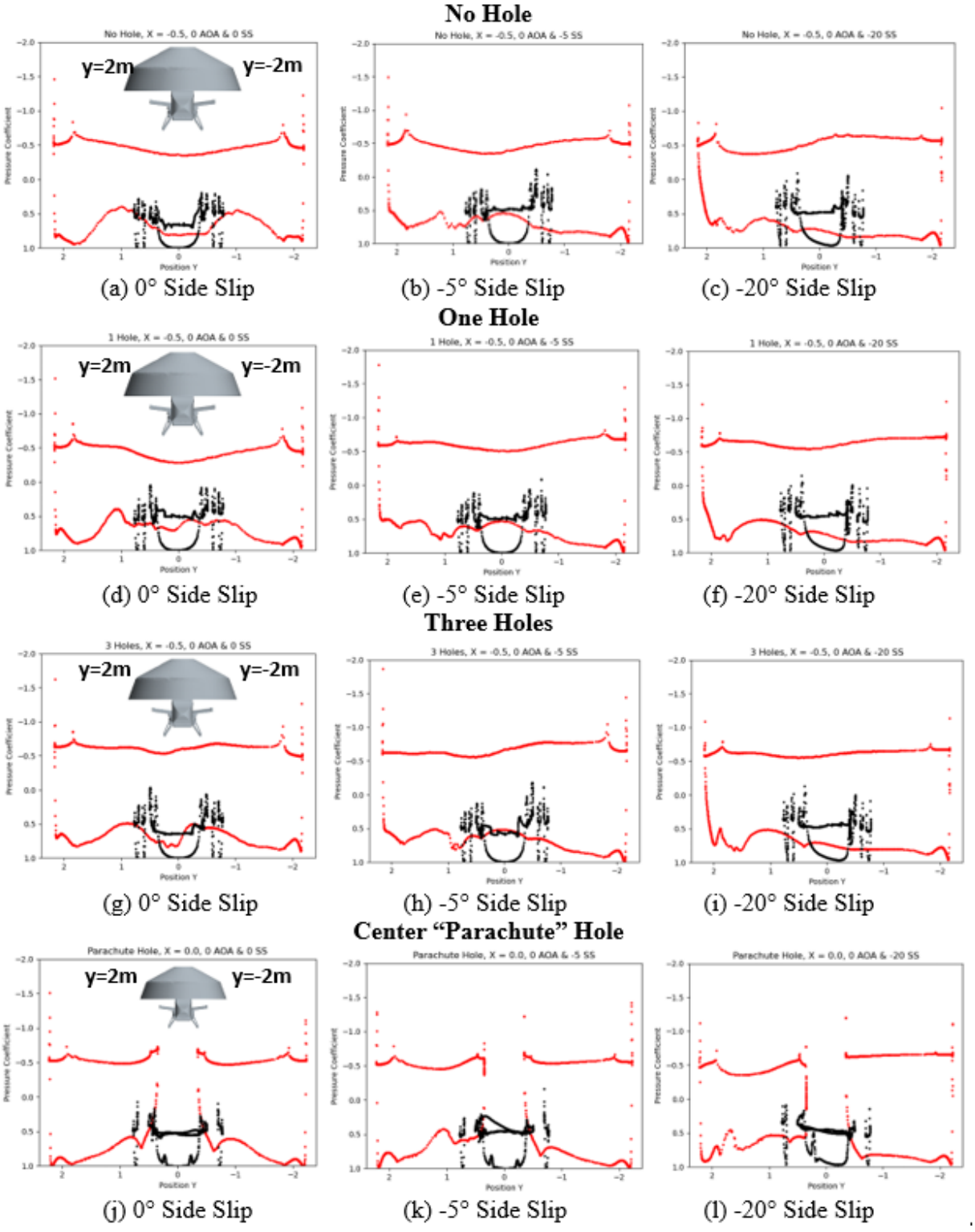

Figure 23: Cp distributions along the surface of the backshell (red) and lander (black) at X = -0.5m

3.1.2 Backshell Separation

To corroborate the findings in the vent trade study and establish whether the suction torque moment was truly independent of the backshell, an analysis was conducted posing the lander at varying separation distances. Eight different posed configurations were evaluated with increasing separation between Dragonfly and its backshell. These scenarios are illustrated in Figure 27. Separation distances ranged from the original posed configuration to a span of 20m, which was predicted to be far enough downstream to display no interaction between lander and backshell.

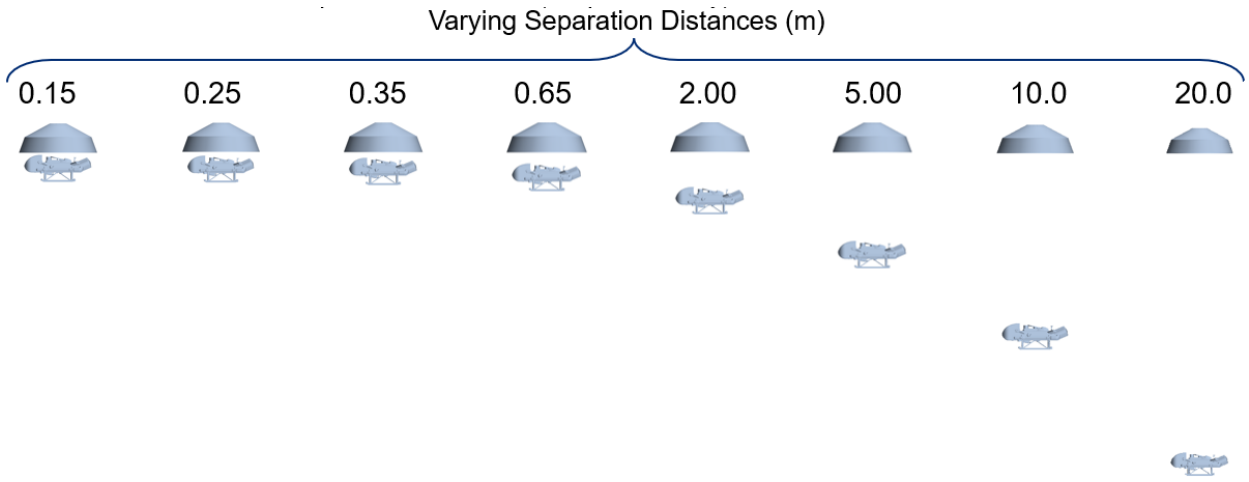

Figure 24: Dragonfly posed at various separation distances

Figure 25 presents the despin moment as a function of separation distance with a positive sign convention defining a clockwise, nose right rotation. Rotors 6 and 8 were used as the controlling rotors, corresponding to the bottom-fore-starboard rotor and the bottom-aft-port rotor, respectively. As predicted from the previous study, the backshell remained independent of the despin moment with a constant zero value across all separation distances. The suction torque, equivalent to the Dragonfly body Z-moment, was clockwise at each separation distance, whereas the rotor torque moment resulted in an opposing counterclockwise, nose left rotation at each

separation distance. This infighting between the two moments highlights the lack of control authority necessary for despinning the system during PPF. In other words, the direction of the suction torque moment opposed the direction of the rotor torque moment at each separation distance, resulting in the suction torque effectively canceling out the moment generated by the controlling rotors. The summation of all three moments was approximately zero, thus depriving the system of any method to reduce system spin following heatshield release. The findings also show the suction force was not a strong function of the separation distance from the backshell. At roughly 10*m* there was only a 25% reduction in the suction force, which remained similar in magnitude to the opposing rotor torque. These findings support backshell independence with respect to the suction force at increasing separation distances.

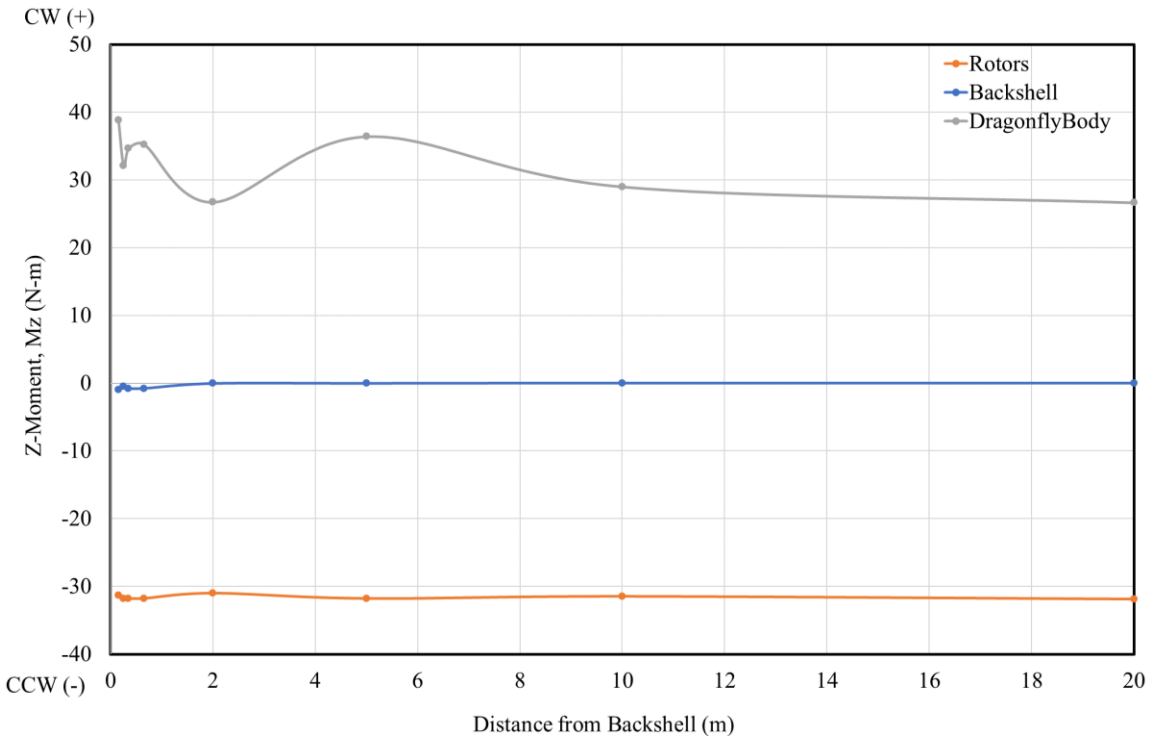

Figure 25: Despin moment as a function of backshell distance for the backshell, lander body, and rotors

Figure 26 provides a starboard and port side visualization of the suction force with respect to the controlling rotors at separation distances of 2*m* and 5*m* away from the backshell. The blue shading represents a negative pressure coefficient on the lander body and corresponds to a suction force towards the nearest adjacent rotor. The largest suction force distributions were located at the front starboard "nose" and aft port "tail" of the lander, aligning with the locations of controlling rotors 6 and 8. The result was an induced clockwise rotation of the lander body, corroborating the findings shown in Figure 25.

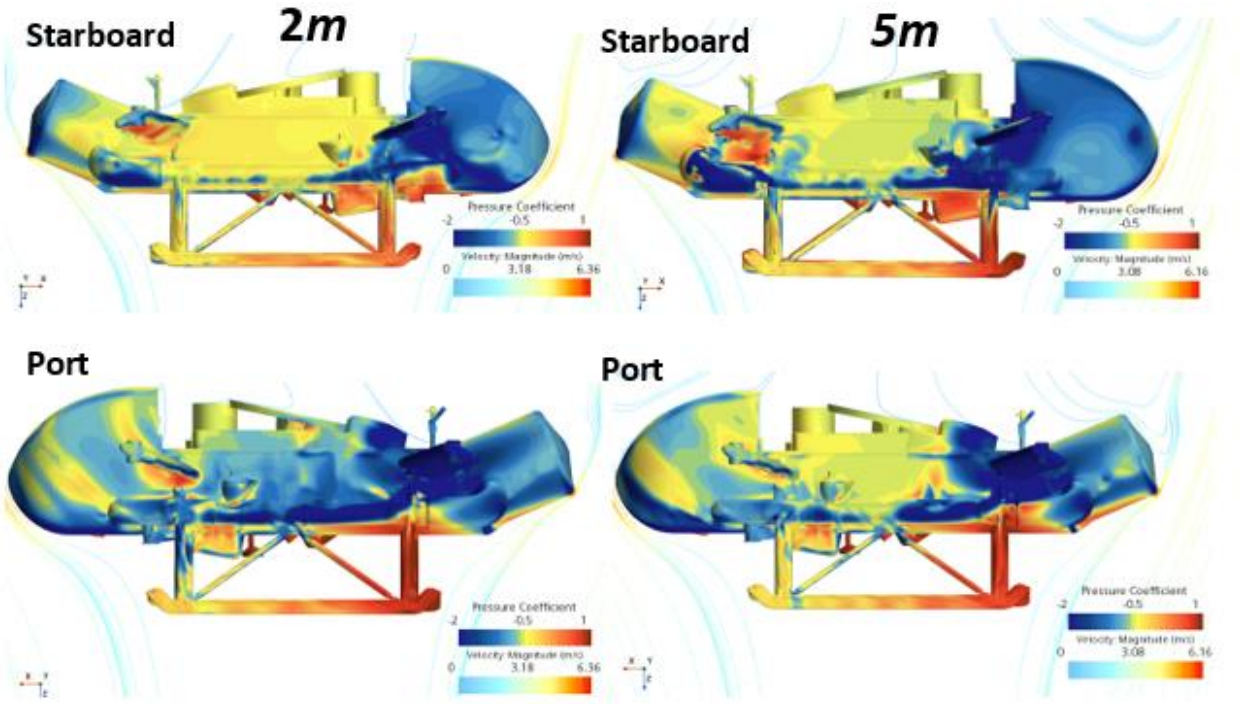

Figure 26: Surface pressure distributions for Dragonfly at 2m and 5m

The implementation of two potential mitigation strategies, namely venting the backshell and increasing the separation distance, were evaluated for their effectiveness in reducing or eliminating the impact of the suction torque on the lander-backshell system. The results indicated that neither approach had significant potential in achieving this objective. Overall, Dragonfly's

backshell was deemed independent of suction torque and produced no significant effect on despin capabilities; therefore, diagnosing the cause of the suction force and developing alternative methods for control was imperative for successful despin prior to lander release.

3.2 Rotor Configurations: Isolated Single Rotors

The initial objective of Dragonfly PPF was to generate a comprehensive aero-database covering a wide range of descent scenarios, which enmcopassed variations in the angle of attack, side slip, free stream descent velocity, rotor speed settings, and controlling rotor configurations. The resulting database revealed a significant issue concerning the failure of the system rotation to conform to the expected rotor dynamics, particularly in the Z-moment or despin direction. In specific instances, Dragonfly in its posed configuration, did not rotate in the direction opposite of the controlling rotors as expected. In fact, these cases of concern displayed a system rotation in the same direction as the rotor torque leading to a loss of control. The issue stemmed from an unexpected suction torque which induced an additional moment on the system in the direction opposite of the controlling rotors. One such scenario occurred when controlling Dragonfly with rotors 6 and 8 as encountered in the separation study. This was of particular concern, because NASA defined this rotor pair as the two controlling rotors for despin. Therefore, the conventional method of control (i.e. using rotor torque) was not satisfactory in preventing system rotation after releasing the heatshield. The focus of this continued research was to develop a better understanding of the suction torque and explore alternative strategies for restoring control authority. With a more thorough grasp of the suction torque, this effort was able to provide feasible solutions to address the challenges associated with despin.

3.2.1 Starboard Rotors

The present study will focus exclusively on the posed configuration, as the rotors in the stowed configuration do not have sufficient clearance to power on. After separation of the heatshield, Dragonfly decelerates to an acceptable velocity before extending to its posed configuration. At this point, the controlling rotors are activated. As a subset of the larger aero-database, bottom rotors 6 and 8 were swept from 100 RPM to 1100 RPM, while the remaining rotors were fixed at 100 RPM. Based on the location of these two rotors, referenced in Figure 19, a system rotation opposite to the rotation of the controlling rotors was expected. As viewed from above, rotors 6 and 8 were assigned a clockwise rotation resulting in an expected system rotation in the counterclockwise direction, increasing with RPM. The expected rotation is illustrated in Figure 27. This characteristic was not universally observed and highlighted the unexpected lack of control authority about the wind-frame z-axis. Specifically, these cases show a behavior in which the system rotated in the same direction as the controlling rotors. The current section presents a study that examines the impact of each starboard side rotor by individually sweeping the rotor speed from 200 RPM to 600 RPM and identifying the effect on the total despin moment.

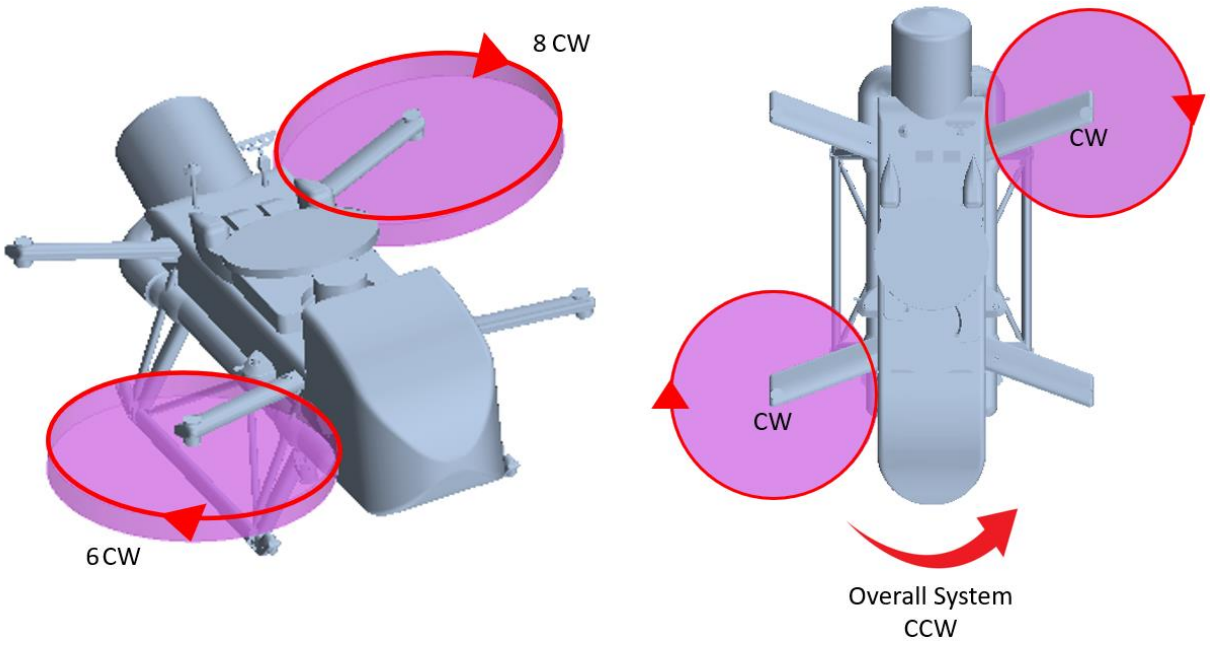

Figure 27: Expected rotation of Dragonfly when controlled with CW spinning rotors

Figure 28 shows the breakdown of the total Z-moment into individual rotor and lander contributions as a function of rotor speed (RPM). It is important to note, the plots designate a clockwise moment as positive and a counterclockwise moment as negative. The analysis of top rotors 1 and 4 indicated the rotor torque was effectively negated by the moment generated from the rotor thrust, as evidenced by the magnitude of the orange trendline. For instance, rotor 1 was designated with a counterclockwise rotation, thus the system should expect a resultant clockwise moment generated from the rotor torque; however, the inward cant angle of the rotor produced a thrust which created a counterclockwise moment. The clockwise moment from the rotor torque and the counterclockwise moment from the rotor thrust resulted in an overall rotor moment near zero. This resulted in a negligible contribution of the rotors to the rotational behavior of the system. The cancellation of these moments was directly linked to the front starboard location of rotor 1, which led to a nose left thrust. This implied that Dragonfly's total despin moment was highly

dependent on the aerodynamic forces and surface pressures on the lander body only. The resulting lander moment is referred to as the suction torque. Standard control authority for rotorcrafts typically observes a vehicle rotation in the direction opposite of the controlling rotors as a direct result of the rotor torque. Alternatively, a unique method of control authority can be achieved when system control is obtained using only the suction torque rather than the rotor torque. This second method of control was successfully attained when using rotors 1 and 4 as the powered rotors. It is important to emphasize for rotors 1 and 4, the control direction remained opposite of the controlling rotor spin as was originally expected. For example, rotor 1 rotated counterclockwise with a resulting overall system moment in the clockwise direction. Additionally, both rotors 1 and 4 effectively eliminated the influence of rotor torque on the despin moment, maintaining system control with the suction force only.

For bottom rotors 6 and 7, the moment produced by the rotor torque and the moment generated by the cant thrust became additive. This was indicated by an increase in the counterclockwise (-) direction for rotor 6 and an increase in the clockwise (+) direction for rotor 7. Rotor 6 was located coaxially beneath rotor 1 and designated with a clockwise rotation; therefore, a counterclockwise system rotation was expected. Like rotor 1, the cant of rotor 6 produced a nose left force component resulting in a counterclockwise moment. The two components of the total rotor moment now agreed. Despite the additive contribution from the rotors being counterclockwise as desired, the lander body experienced a dominating suction torque which pulled the lander nose left in the opposing clockwise direction. This highlighted the underlying control issue uncovered in the posed aero-database. The lander suction torque was in opposition to the rotor torque. This opposing rotational behavior manifests as a conflict between moments, thereby leading to an absence of system control.

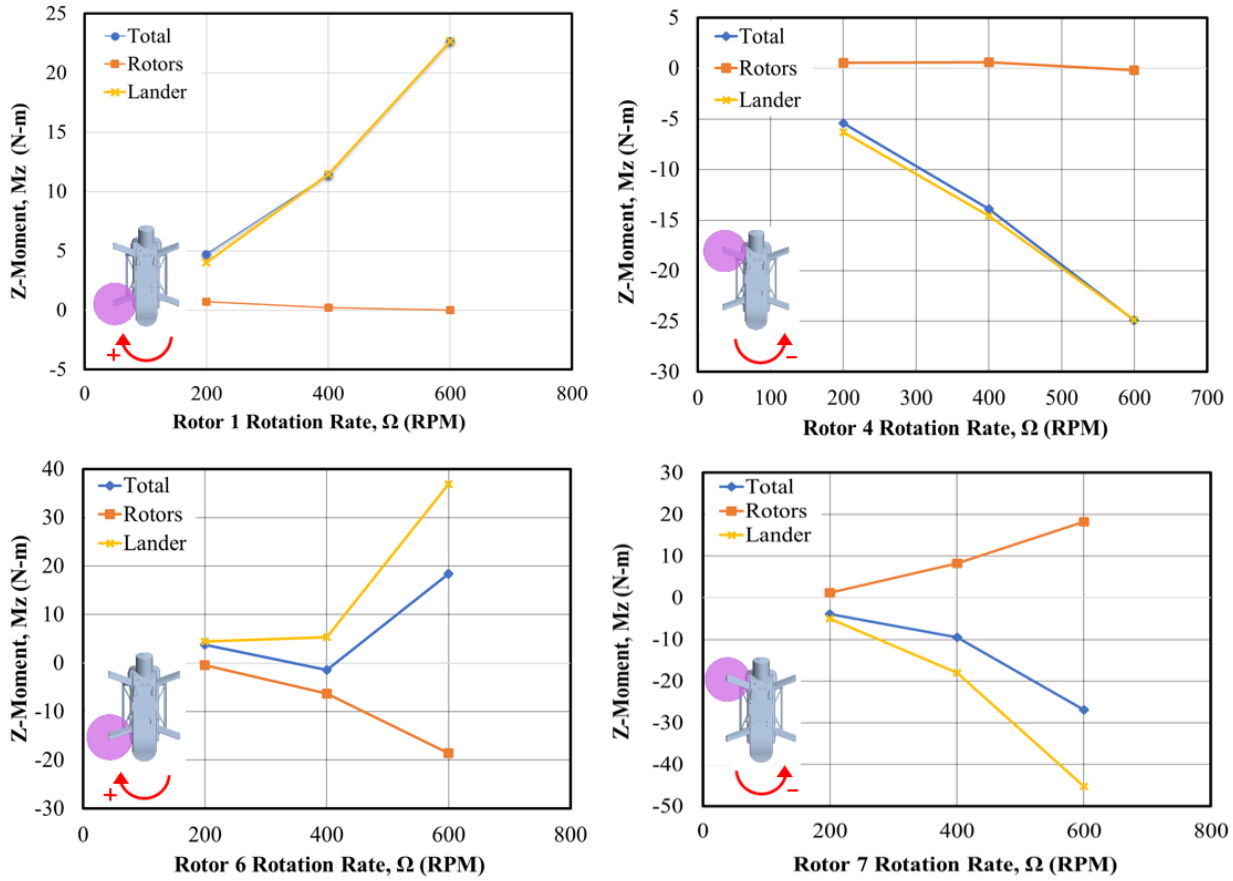

Figure 28: Total, rotor, and lander Z-moments for each starboard rotor
(Control authority indicated by monotonically increasing values in the total moment)

The suction torque produced between the controlling rotor and lander body was the primary cause of the observed phenomenon. Without the suction torque, the system would follow conventional control methods for a slim-body rotorcraft. For example, without a suction force rotors 6 and 7 would consist of only a rotor torque in the direction opposite to the rotor spin. The suction force was attributed to a downward flow, or downwash, generated by the rotor thrust. This in turn, produced a negative surface pressure on the side of the lander nearest to the controlling rotor. This rotor-body interaction exerted a "pulling" effect on the lander towards the controlling rotor itself. This effect was observed for all starboard rotors and was solely dependent on the rotor

location. Rotors 1 and 6, located fore-starboard of Dragonfly, pulled the lander nose to the right in the clockwise direction. Rotors 4 and 7, located aft-starboard of Dragonfly, pulled the lander tail to the right in the counterclockwise direction. This result is supported by the yellow trendlines shown in Figure 28. While this effect was observed for all starboard rotors, the suction force had an adverse impact on rotors 6 and 7 as previously discussed. For rotor 6 specifically, the rotor downwash produced a negative pressure coefficient on the front starboard side of the lander body, thus pulling the nose to the right and generating a clockwise rotation. This was problematic given the suction force generated a moment opposite to the rotor torque, and the resulting moment direction agreed with the spin designation of rotor 6. This effect is illustrated in Figure 29 by visualizing the surface pressure contours on each side of the lander body. The pressure contour scenes indicated lower pressure coefficients on the starboard side of the lander near the controlling rotors and higher pressure coefficients port side. It is crucial to emphasize the direction of rotation, resulting from the negative surface pressure coefficients, was towards the controlling rotor(s). These findings underscore the need for additional strategies for despin. As previously stated, despin is essential in stabilizing Dragonfly after heatshield separation and has become a major focus of current design efforts. These findings suggest that employing rotor 1 or rotor 4 would yield more effective control authority, attributed to the elimination of conflicting Z-moments. Although traditional quadrotor control is not achieved via rotor torque, the system maintains control authority by taking advantage of the suction torque.

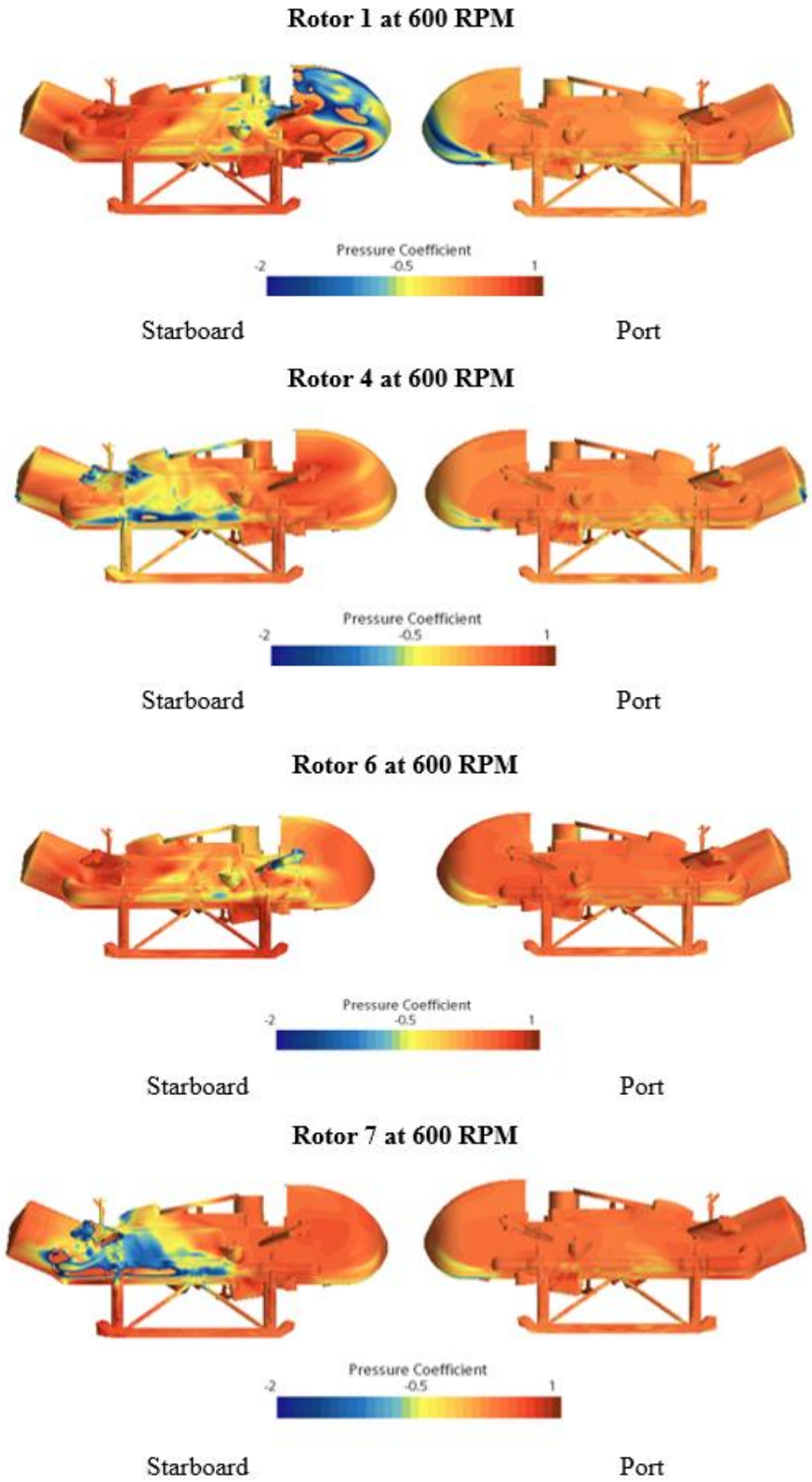

Figure 29: Surface pressure contours displaying pressure differences caused by suction force

3.2.2 Port Rotors

To provide a comprehensive analysis and ensure the results were consistent on both sides of the lander body, the research was extended by replicating the previous effort on Dragonfly's port side. One notable distinction between the port rotor simulations and the starboard rotor study was the rotational velocity of the controlling rotors. In this study, each individual controlling rotor was limited to 600 RPM, while the remaining rotors were fixed at 100 RPM. Similar to the starboard simulations, rotor 2 and rotor 3 experienced a moment cancellation between the rotor torque and the moment generated by the cant thrust. This was a direct result of the rotors locations relative to the lander body. Rotor 2 was situated at the front port side of the lander and was characterized by a clockwise rotational motion, which in turn generated a rotor torque directed in the counterclockwise direction. At this location, a thrust component "pushed" the lander nose to the right in a clockwise direction. The resulting moments were in opposition, as seen previously with rotors 1 and 4 on the starboard side of the lander body. The rotor moment cancellation is shown in Figure 30 and emphasized by the circled Z-moment values. In keeping with prior observation, this left the control authority solely up to the lander Z-moment, or suction torque. The lateral placement of rotor 2 initiated a suction force on the nose of lander corresponding to a "pulling" effect in the counterclockwise direction. This agreed with previous findings. Like starboard rotor 1, rotor 2 achieved rotor control in the direction opposite to its spin by taking advantage of the suction torque.

The outcomes obtained when studying the effects of rotors 5 and 8 bear resemblance to those obtained when examining rotors 6 and 7. The rotor Z-moment and the lander Z-moment were observed in opposite directions of rotation; therefore, both influenced the total system moment, or

despin moment. Given its orientation in relation to the lander body, rotor 5 produced a suction torque in the same counterclockwise direction as rotor 2. Note, rotor 5 was located coaxially beneath rotor 2. In contrast to rotor 2, rotor 5 was designated with a counterclockwise rotation, leading to a rotor torque in the clockwise direction. As such, the torque generated from the rotor and the moment produced by the thrust component were additive. Here, the rotational moment of the suction torque and the rotor moment acted in opposition, leading to insufficient control authority. This diametrically opposed effect is shown in Figure 30.

It became evident from the individual rotor analyses why control issues related to despin were encountered by rotors 6 and 8 during PPF. Traditional rotor control methods proved ineffective due to the rotational direction and location of these rotors. The creation of a suction force from the rotor downwash led to a nose rotation towards rotor 6 and a tail rotation towards rotor 8. The resulting clockwise moment counteracted the rotor torque moment, which led to non-monotonic behavior in the total despin moment. In the absence of the suction force, the rotor torque would have enabled successful rotational deceleration of the system. Although it is not a traditional method of controlling rotorcraft, the results show the suction torque could be used to regain control authority. Transitioning to controlling rotor pairs 1 and 3 or 2 and 4 would see significant improvements in rotor control. Of these two options, implementing rotors 1 and 3 would allow rotor control in the traditional direction opposite to their respective rotor spin designations.

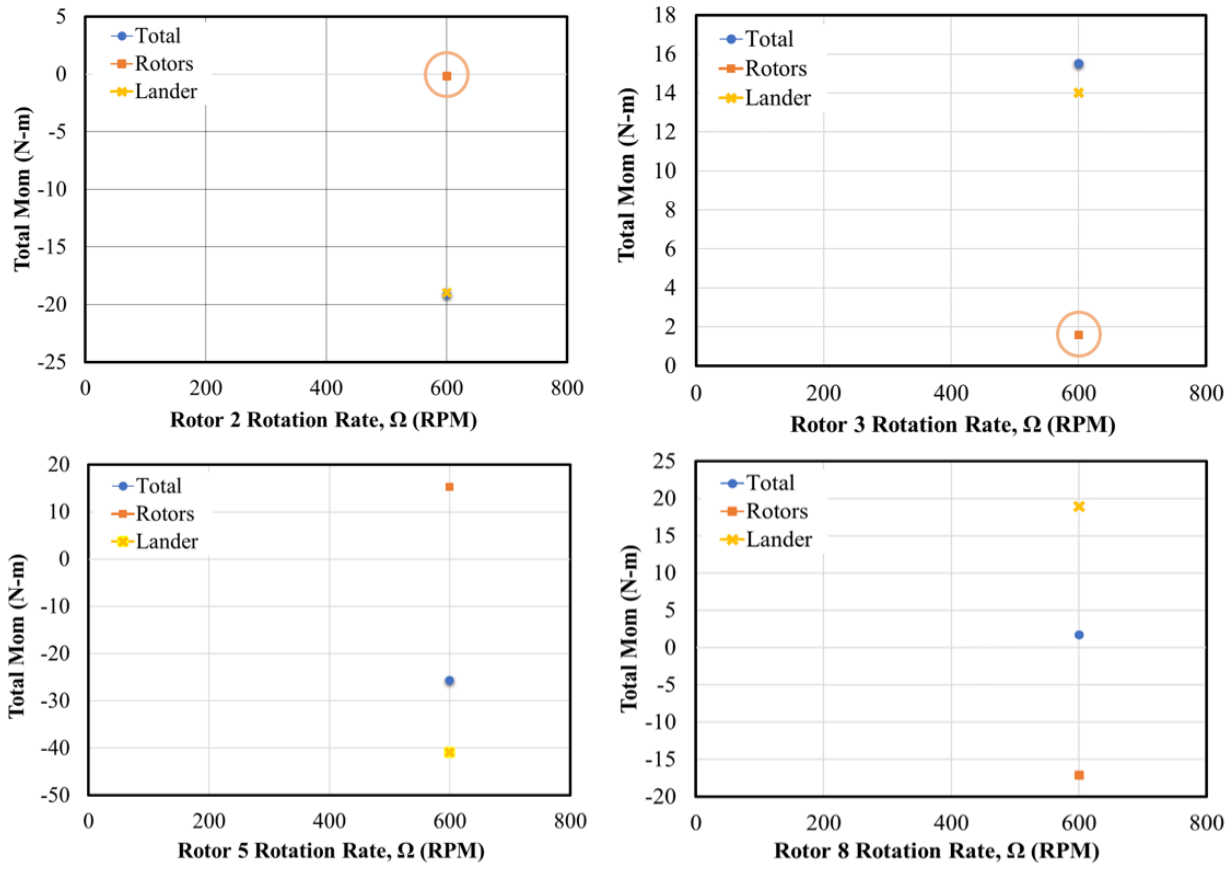

Figure 30: Total, rotor, and lander Z-moments for each port rotor
(Control authority indicated by monotonically increasing values in the total moment)

3.3 Rotor Cant: Two Rotor Control Study

The objective of this study was to evaluate the impact of rotor cant on suction torque, with the aim of improving the despin maneuver. As indicated by previous findings, the change in aerodynamics brought about by lateral cant had a significant impact on the overall rotor torque experienced by the system. Rotors 6 and 8, which were initially constrained as the controlling rotors, are used in the present study at rotor speeds varying from 200 RPM to 600 RPM. Dragonfly's current configuration features a 5-degree lateral cant inwards for each rotor, which produced a thrust in the counterclockwise direction when using the controlling rotors. The thrust vector and expected system rotation are illustrated in Figure 31. The relationship between the

moment generated from thrust and the moment generated from the controlling rotor torque was analyzed in the isolated rotor simulations and found to have an additive effect in the counterclockwise direction. The previous study also concluded that the suction torque opposed this rotation, resulting in a motion towards the controlling rotor. The additive and nullifying effects of the rotor torques may be altered by adjusting the angle of the rotor cant. Increasing the inward cant angle is expected to increase the rotor moment in the counterclockwise direction; however, it may also lead to an increase in the opposing suction torque in the clockwise direction. If an increase in both the rotor moment and suction moment were to occur, there would be no benefit to increasing the inward cant. Conversely, an outward cant angle would be expected to generate a moment in the same direction as the suction force for rotors 6 and 8. This modification would flip the direction of the thrust and counteract the moment produced by the rotor torque. This would allow Dragonfly to take advantage of the suction torque for system control, as seen previously using rotors 1 and 3, and 2 and 4. This study analyzed the effect of lateral cant on the total rotor moments and the lander moments to identify a scenario where the two were in agreement. If the outward canted rotors can produce enough thrust to overcome the rotor torques, it is theoretically possible for the total rotor moment and the lander suction torque moment to be in the same direction.

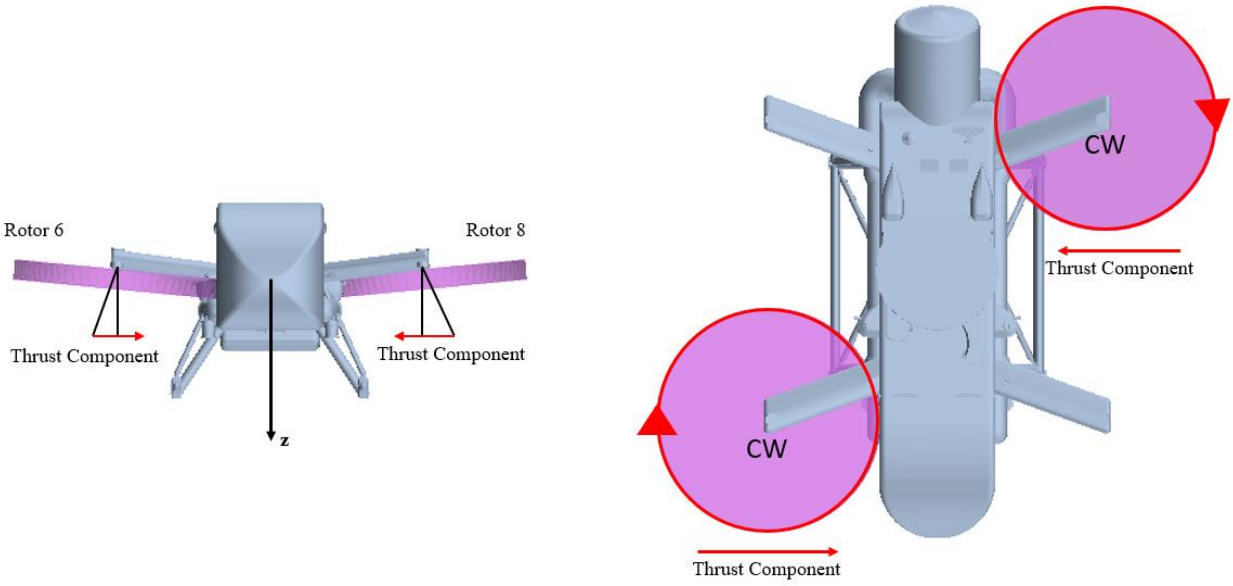

Figure 31: Thrust components of rotors 6 and 8 for a 5-degree inward cant

Three separate rotor cant angles were examined during free stream descent to observe their impact on the total despin moment of the system. Cant angles of 5 degrees inwards, 0 degrees, and 5 degrees outwards were selected, and the resulting rotor, lander, and system Z-moments were computed for each angle as a function of the rotor RPM. Figure 32 shows the contributing moment from the combination of rotor torque and component thrust for each cant angle. When Dragonfly was configured with the original inward cant angle, the rotor torque and thrust component generated a moment in the same direction becoming additive in the counterclockwise direction. Such behavior was consistent with the results of previous efforts. With no applied cant angle, only the rotor torque contributed to the rotor moments. The resulting system rotation was counterclockwise, as expected from quadrotor dynamics, but was lower in magnitude due to the elimination of the thrust component. Reversing the cant alignment to an outward orientation led to a reversal in the direction of the thrust component, resulting in a thrust force that opposed the the rotor torque.

Figure 33 shows the lander Z-moment, or suction force, contribution to the overall system despin moment. For every cant angle, the lander moment increased in the clockwise direction with increasing RPM. This trend indicated that the suction force was independent of cant angle and relied only on the position of the controlling rotors. In other words, the rotor-lander interaction induced by the rotor downwash was not a strong function of the cant angle. To achieve control authority, the rotor Z-moment must become greater than or equal to zero.

The combined rotor and lander contribution to the overall moment are presented in Figure 34. A prescribed inward cant angle led to adverse conditions where Dragonfly rotated in the same direction as the controlling rotors and in opposition to the suction torque. This resulted in a reduced capability to despin Dragonfly during PPF. The same issue persisted when the cant angle was reduced to zero. The moment contribution of the rotor torque remained counterclockwise opposing the suction torque. The outward canted rotors were the only configuration that resulted in a positive clockwise moment matching the suction force and resulted in monotonic behavior in the total Z-moment. Overall, outward canting rotors 6 and 8 offered the highest level of control authority because the rotor, lander, and total despin moments were all positive in the clockwise direction and increasing with RPM. It is noteworthy to reiterate, the direction of control authority corresponded to the spin direction of the controlling rotors in this scenario, which is not the traditional convention for controlling rotorcraft vehicles. Typically, rotorcrafts are controlled by spinning counter to the direction of the high-powered rotors. However, in this configuration Dragonfly was able to exploit the strong suction forces generated by the rotor-body interactions to achieve controlled despin.

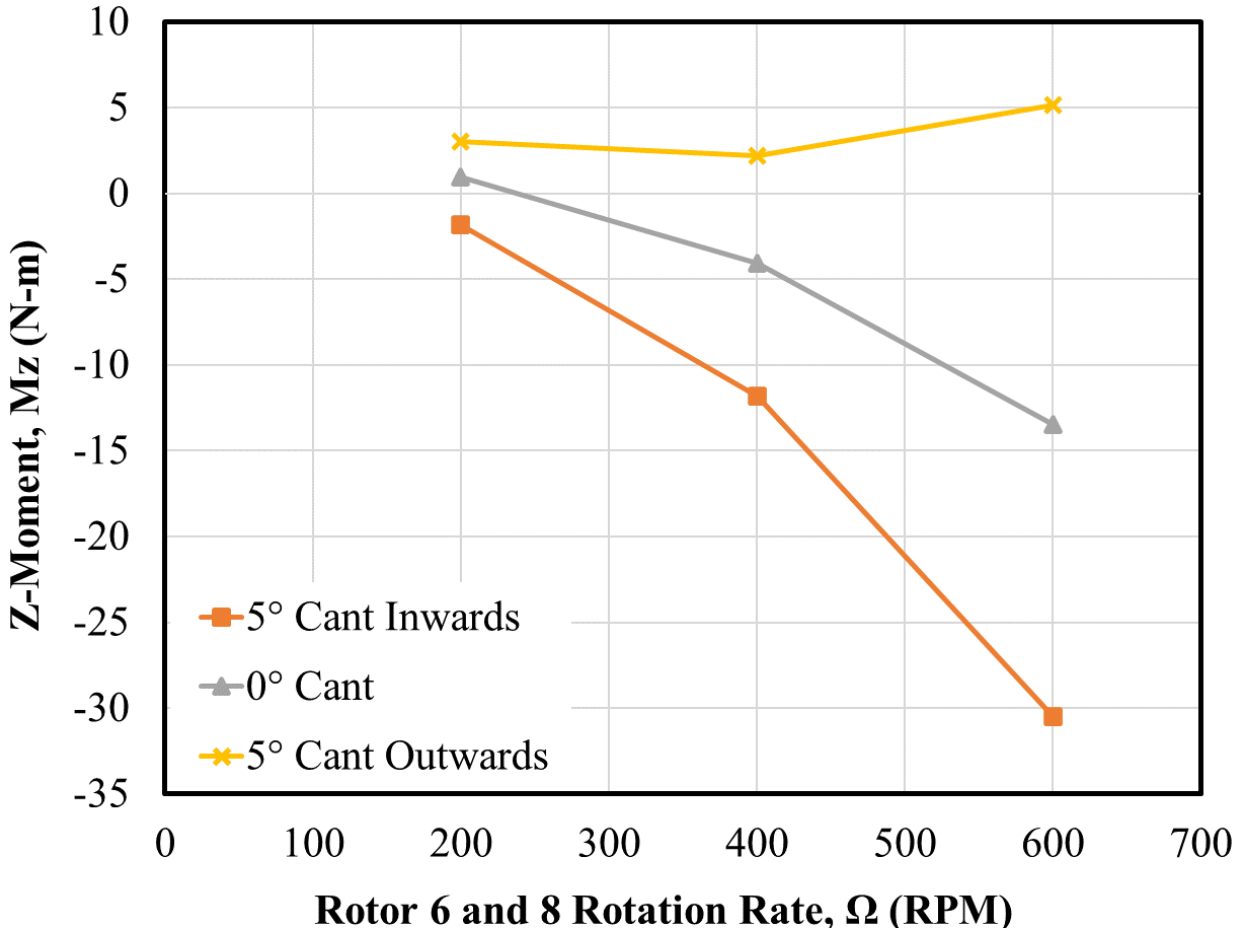

Figure 32: Rotor moment for each cant angle as a function of controlling rotor RPM

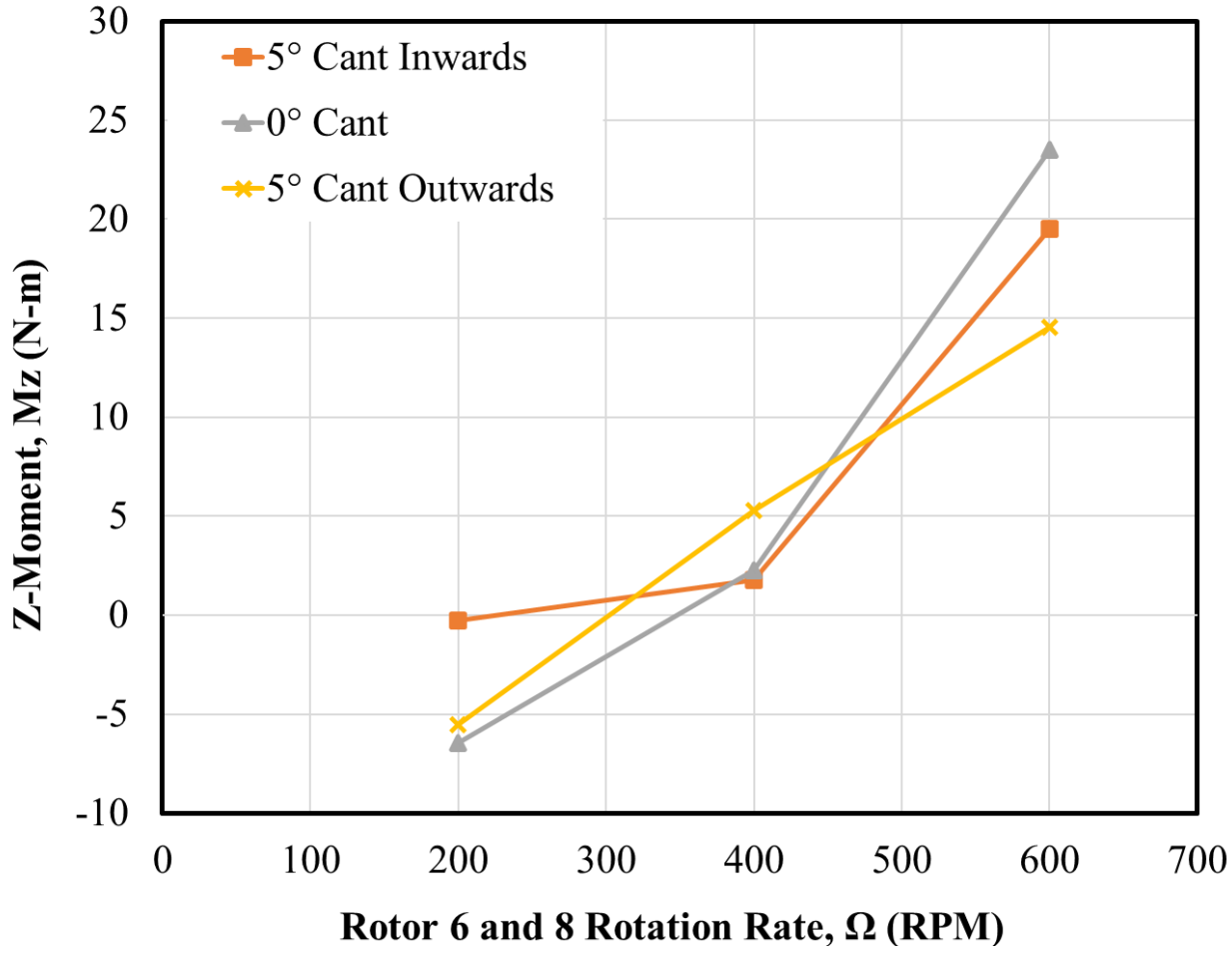

Figure 33: Lander moment (suction torque) for each cant angle as a function of controlling rotor RPM

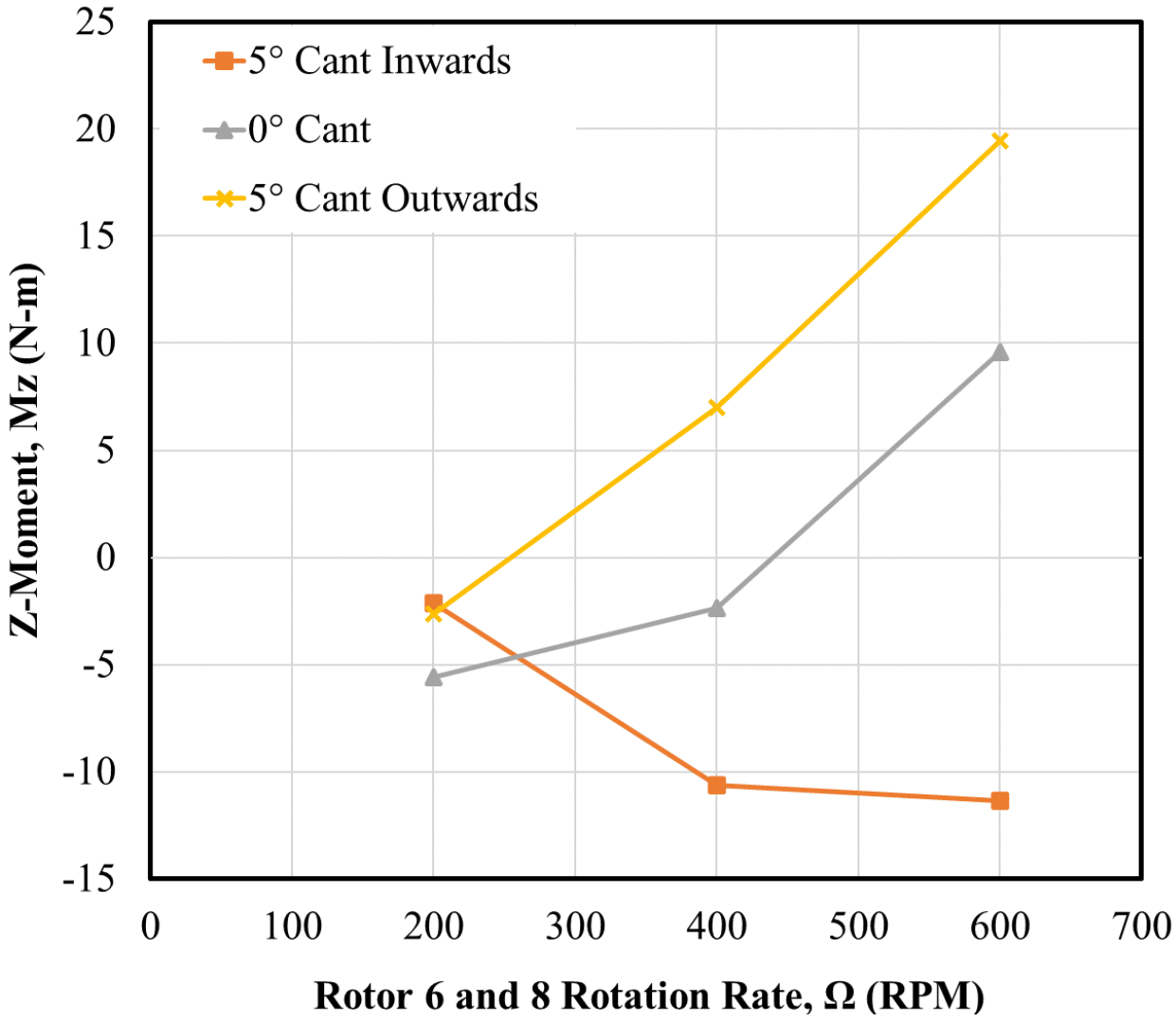

Figure 34: Total moment for each cant angle as a function of controlling rotor RPM

CHAPTER 4: CONCLUSION

This paper presented an analysis of Dragonfly's aerodynamic performance during PPF on Titan, from heatshield separation up to lander release from the backshell guiderails. The mission scope and challenges experienced during rotorcraft descent were presented in the context of a non-terrestrial atmosphere. The fundamental goals of this research included improving confidence in the CFD models and numerical solvers through benchmark comparisons, identifying the cause of instabilities found in the aerodynamic database, documenting lander-backshell interaction and its influence on flow character, and proposing solutions to achieve greater control authority prior to lander release.

To reinforce dependability of the CFD results, three benchmark simulations were carried out to evaluate StarCCM+'s capability in reproducing experimental data. To provide context for the selected numerical solvers, a brief background of the software was provided. Experimental studies targeting the MER backshell, Ahmed bluff body, and Robin body were selected for comparison because their geometries were representative of Dragonfly's backshell, bluff lander body, and rotor interaction, respectively. Mesh independence was ensured prior to each benchmark by selecting a cell-reference size that balanced the computational run time and discretization error. In the first study, the aerodynamic lift, drag, and pitch moment coefficients were computed and compared against experimental wind tunnel test data for the MER backshell over a range of angles of attack. The backshell was rotated about its pitch axis from -10 degrees to 90 degrees angle of attack. The CFD coefficients computed for lift and drag closely aligned with the experimental results. The trend in pitch moment was consistent with the experimental data; however, the RANS model showed a slight negative bias and the URANS model slightly underpredicted the coefficient value. Despite the presence of this discrepancy, the aerodynamic coefficients were highly

congruent with the experimental data. The second study used the same mesh independence and benchmarking procedure when comparing the CFD results of the Ahmed body to experimentally published data. The simulation evaluated consequent flow separation and drag characteristics of the body when varying the slant angle at its rear from 0 degrees to 30 degrees. The results indicated that each computational model accurately reflected the expected trend in drag behavior when altering the slant angle. As found experimentally by S. R. Ahmed, the 30-degree slant angle was identified as the transition point for flow separation. For the third benchmark analysis, the experimental setup for the ROBIN body was reproduced in the CFD environment and steady-state surface pressure and load data was obtained for various advanced ratios and thrust coefficients. The overall flow along the fuselage was well captured, and the surface coefficients aligned well with the experimental results across different advance ratios. Using the information gathered from these studies, the lower computational cost RANS model was deemed optimal for generating the required data for generating aerodynamic tables and expanded data sets. The higher fidelity URANS model was used sparsely to spot check the quasi-steady results.

A base simulation was developed for Dragonfly in free-stream descent, during its stowed and posed configurations, to generate an extensive aero-database covering various flight conditions. A subset of the data revealed an instability in which the controlling rotors failed to achieve control authority. In other words, the system was not capable of successfully “despinning” after the heatshield was jettisoned. The main focus of the first two studies was to determine the influence of the backshell on the flow character experienced by the lander. The first study investigated the effect of venting the backshell on the resulting flow behavior for different venting configurations, or hole placements. No significant changes in despin restoring moment were observed between the different configurations and there was no impact on the instability; however,

the study did reveal that an asymmetric hole placement produced undesired moments at zero angle of attack and side slip. Switching from the current one-hole configuration to a symmetric configuration does not solve the despin control issue; however, it would improve the overall stability of the lander in descent. The second study expanded on this idea of backshell independence by incrementally increasing the separation distance between the backshell and lander body. When powering Dragonfly with controlling rotors 6 and 8, the rotors induced a negative counterclockwise moment on the system and the suction force induced a positive clockwise moment on the system. These two moment contributions remained in opposition regardless of Dragonfly's position relative to the backshell. The suction force was not a strong function of separation distance from the backshell and supported the previous findings of backshell independence from the instability. Isolated rotor studies were conducted for each individual rotor on both the starboard and port side of the lander body. The aim of this research was to observe the impact of each rotor on the overall system Z-moment and pinpoint the instability. The results uncovered a suction force generated from rotor downwash interacting with the side of the lander body nearest the controlling rotor. This force produced a suction torque and moment in opposition to the controlling despin rotors. Alternative rotor configurations, such as rotors 1 and 3, offered better control authority because they eliminated the rotor thrust component and took advantage of the strong moment induced by the suction torque. Alternatively, changing the cant angle of rotors 6 and 8 from an inward facing cant to an outward cant would achieve the same result. The switch to an outward facing cant sets the thrust component in opposition to the rotor torque and effectively eliminates the rotor's influence on Dragonfly's rotation. It is important to note that both proposed solutions achieve control authority; however, they do not follow the traditional convention for controlling rotorcraft vehicles. Rather than using the torque of the rotors to control the system

rotation, these methods take advantage of the strong suction force generated from the rotor-lander interaction. Research is still ongoing for Dragonfly descent during PPF with planned experimental studies to verify these findings.

LIST OF REFERENCES

[1] "Solar System Exploration: Titan," Dec. 06, 2022. https://solarsystem.nasa.gov/moons/saturn-moons/titan/exploration/?page=0&per_page=10&order=launch_date+desc%2Ctitle+asc&search=&tags=Saturn&category=33#dutch-astronomer-christiaan-huygens-discovers-titan (accessed Dec. 07, 2022).

[2] J. K. Cornelius *et al.*, "Dragonfly - Aerodynamics during transition to powered flight," in *77th Annual Vertical Flight Society Forum and Technology Display, FORUM 2021: The Future of Vertical Flight*, 2021. doi: 10.4050/f-0077-2021-16698.

[3] J. W. Langelaan, S. Schmitz, J. Palacios, and R. D. Lorenz, "Energetics of rotary-wing exploration of Titan," in *IEEE Aerospace Conference Proceedings*, 2017. doi: 10.1109/AERO.2017.7943650.

[4] M. J. Wright *et al.*, "Dragonfly Entry and Descent System," 2019. Accessed: Nov. 30, 2022. [Online]. Available: https://ntrs.nasa.gov/citations/20190028683

[5] C. A. Zucker, L. Amaya, W. Farrell, and M. P. Kinzel, "A Numerical Investigation of the Dragonfly Lander Exiting an Aero Backshell During Descent into Titan," in *AIAA SCITECH 2023 Forum*, Jan. 2023. doi: 10.2514/6.2023-1948.

[6] M. Carreño Ruiz, N. Bloise, E. Capello, D. D'Ambrosio, and G. Guglieri, "Assessment of Quadrotor Near-Wall behaviour using six-Degrees of Freedom CFD simulations," in *AIAA SciTech Forum*, 2023.

[7] NASA, "Entry, Descent, and Landing," *NASA Science: Mars 2020 Mission Perseverance Rover*. https://mars.nasa.gov/mars2020/timeline/landing/entry-descent-landing/ (accessed Nov. 30, 2022).

[8] R. Mineck, "Summary of Wind Tunnel Tests of Scale Models of the Mars Exploration Rover Backshell and Lander," Oct. 2001.

[9] S. R. Ahmed, G. Ramm, and G. Faltin, "Some salient features of the time-averaged ground vehicle wake," in *SAE Technical Papers*, 1984. doi: 10.4271/840300.

[10] E. Guilmineau, "Computational study of flow around a simplified car body," *Journal of Wind Engineering and Industrial Aerodynamics*, vol. 96, no. 6–7, 2008, doi: 10.1016/j.jweia.2007.06.041.

[11] N. Ashton, A. West, S. Lardeau, and A. Revell, "Assessment of RANS and DES methods for realistic automotive models," *Comput Fluids*, vol. 128, 2016, doi: 10.1016/j.compfluid.2016.01.008.

[12] M. R. Yaacob, R. K. Schlander, P. Buchhave, and C. M. Velte, “Experimental evaluation of Kolmogorov’s -5/3 and 2/3 power laws in the developing turbulent round jet,” *Journal of Advanced Research in Fluid Mechanics and Thermal Sciences*, vol. 45, no. 1, 2018.

[13] R. E. Mineck and S. A. Gorton, “Steady and periodic pressure measurements on a generic helicopter fuselage model in the presence of a rotor,” *NASA Tech Memo*, no. 210286, 2000.

[14] J. Cornelius and S. Schmitz, “Rotor Performance Predictions for UAM - Single vs Coaxial Rigid Rotors,” 2022.

[15] “Star CCM+. Simulation of Turbulent Flow in Arbitrary Regions - Computational Continuum Mechanics.” Siemens.

[16] I. Kohri, T. Yamanashi, T. Nasu, Y. Hashizume, and D. Katoh, “Study on the Transient Behaviour of the Vortex Structure behind Ahmed Body,” *SAE International Journal of Passenger Cars - Mechanical Systems*, vol. 7, no. 2, 2014, doi: 10.4271/2014-01-0597.